

Generalizing GNNs with Tokenized Mixture of Experts

Xiaoguang Guo¹, Zehong Wang², Jiazheng Li¹, Shawn Spitzel¹, Qi Yang¹,
Kaize Ding³, Jundong Li⁴, Chuxu Zhang^{1,†}

¹University of Connecticut ²University of Notre Dame ³Northwestern University ⁴University of Virginia

xiaoguang.guo@uconn.edu, zwang43@nd.edu, jiazheng.li@uconn.edu, shawn.spitzel@uconn.edu, qiyang942@gmail.com, kaize.ding@northwestern.edu, jundong@virginia.edu, chuxu.zhang@uconn.edu

†Corresponding Author

Abstract

Deployed graph neural networks (GNNs) operate as frozen snapshots, yet must simultaneously fit clean data, generalize under distribution shifts, and remain stable against input perturbations—three goals that are difficult to satisfy at once with a single fixed model. We first show theoretically that applying the same computation to every input creates a fundamental tradeoff: to resist perturbations, the model must limit how much it relies on shift-sensitive features, which leaves an irreducible floor on worst-case generalization error. Input-dependent routing—assigning different computation paths to different inputs—can break this ceiling, but brings new fragility: distribution shifts may misguide routing decisions, and perturbations cause the routing itself to fluctuate, compounding downstream errors. We formalize these effects through two risk decompositions that separate (i) how well the available paths cover diverse test conditions from how accurately the router selects among them, and (ii) how sensitive each fixed path is from how much routing fluctuation amplifies that sensitivity. Guided by these analyses, we propose **STEM-GNN**: Stable TokEnized Mixture-of-Experts GNN, a pretrain-then-finetune framework that couples a *mixture-of-experts encoder* providing diverse computation paths to cover heterogeneous test conditions, a *vector-quantized token interface* that maps encoder outputs to a discrete codebook to absorb small routing fluctuations before they reach downstream layers, and a *regularized prediction head* that bounds how much the output can amplify any residual upstream variation. Experiments on nine benchmarks spanning node, link, and graph tasks show that STEM-GNN achieves the best three-way balance, improving generalization under degree and homophily shifts and stability under feature masking and edge deletion, while maintaining competitive performance on clean graphs. The code and data are available at <https://anonymous.4open.science/r/STEM-GNN-C814>.

1 Introduction

Graph neural networks (GNNs) have been applied to many real-world systems, powering applications from recommendation and information retrieval to molecular property prediction and knowledge reasoning [1, 4, 15, 18, 24, 31, 41]. In production pipelines, GNNs are typically deployed as versioned snapshots that run without parameter updates between releases [3, 21, 43, 65]. During this *frozen deployment* window, the model encounters two distinct sources of mismatch. *Distribution shifts* arise when the test graph is drawn from a different regime than the training data [17]—for example, a molecular model trained on common scaffolds may fail on novel chemical spaces [62]. *Feature and structure perturbations* arise when individual test inputs are corrupted by missing attributes, noisy

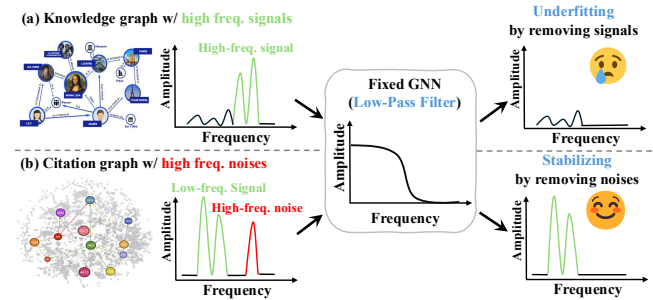


Figure 1: An illustrative example: fixed GNN cannot adapt to diverse deployment scenarios. On a knowledge graph where task-relevant information lies in high-frequency components, a low-pass GNN removes key signals. On a citation graph dominated by high-frequency noise, the same low-pass GNN suppresses noise and improves stability. No single static computation rule resolves both cases simultaneously.

interactions, or mild edge rewiring while remaining semantically close to their clean counterparts [23, 77]. Because the model cannot adapt at test time, strong in-distribution performance, reliable behavior under shifts, and bounded sensitivity to perturbations must all be achieved by a single set of frozen parameters—a tri-objective tension we term the *impossible triangle* of frozen graph deployment.

Prior work has advanced each axis of this triangle largely in isolation. Graph pretraining [9, 20, 47, 51, 53, 55, 74] learns transferable representations that improve clean accuracy and downstream adaptation, yet the resulting model still applies a single fixed forward pass at test time. OOD graph learning [29, 30, 56, 59, 60, 75] targets distribution shifts across environments but often treats perturbation robustness as secondary. Robust graph learning [27, 38, 67, 68, 70, 72, 77] hardens predictors against corruptions but can sacrifice expressivity needed for generalization. Crucially, most methods deploy a *fixed test-time computation rule*: the same message-passing and readout mapping is executed for every input regardless of its characteristics. This raises a fundamental question: *how does the choice of test-time computation mechanism—not just the training objective—govern the tri-objective balance under frozen deployment?*

We adopt the concept of *instance-conditional computation* (ICC) to answer the question: routing different inputs through different mechanisms within a single frozen model [2, 16, 45]. ICC expands the family of effective mechanisms that a frozen parameter set can realize, improving coverage over heterogeneous deployment scenarios (Figure 1). However, ICC also introduces new failure modes. Under distribution shifts, routing decisions can drift, assigning inputs to suboptimal mechanisms. Under perturbations, instability manifests in two complementary ways: (i) even when

the routing decision is unchanged, the executed mechanism may be sensitive to input noise; (ii) perturbations may flip the routing decision itself, switching the executed mechanism and compounding the output variation. Therefore, making ICC robust under frozen deployment requires coupling expanded mechanism coverage with explicit deployment-time stability control—a design goal that existing ICC and MoE methods do not address in graph learning.

We tackle this challenge from both a theoretical and a methodological perspective. On the **theory** side, we formalize static inference (fixed rule) versus ICC under the tri-objective framework and show that: (i) static inference faces a structural limit where a uniform stability budget caps the mechanism’s reliance on perturbation-sensitive parts, creating a floor on worst-environment risk; and (ii) ICC decomposes OOD risk into mechanism coverage and selection quality, and decomposes stability risk into routing-fixed sensitivity and drift amplification, revealing precise levers absent in the static case.

On the **methodology** side, we propose **STEM-GNN**:**S**table **T**ok**E**nized **M**ixture-of-**E**xperts **GNN**, a pretrain-finetune framework that instantiates robust ICC for graph learning through three tightly coupled designs: (1) *MoE Encoder for Coverage Expansion*. A mixture-of-experts message-passing encoder routes each node through an input-dependent combination of shared experts, realizing a family of effective mechanisms under a single frozen parameter set. (2) *VQ Tokenization for Representation Stabilization*. A vector-quantized (VQ) token interface discretizes encoder outputs into a fixed codebook before passing them to the prediction head. Small perturbations that do not cross quantization boundaries produce zero change in the head’s input, absorbing continuous drift and stabilizing the encoder-to-head pathway. (3) *Lipschitz Regularization for Sensitivity Control*. A Frobenius penalty on the prediction head bounds its Lipschitz constant, limiting how strongly any residual change—including discrete token switches—is amplified into output variation. We summarize our contributions as follows:

- **Concept.** We reframe robust graph generalization under frozen deployment as a tri-objective tension and identify the test-time computation mechanism—not the training objective alone—as the key lever governing this balance.
- **Theory.** We formalize static inference vs. ICC under this framework, proving a structural limit of static inference under a stability budget and showing that ICC offers new design levers via coverage-selection and sensitivity-drift decompositions.
- **Methodology.** Based on theoretical analysis, we propose STEM-GNN, a pretrain-finetune framework that couples an MoE encoder, VQ tokenization, and Lipschitz-controlled prediction to operationalize robust ICC for graphs.
- **Experiments.** Experiments on nine benchmarks spanning node, link, and graph tasks show that STEM-GNN achieves the best tri-objective performance, improving OOD generalization and perturbation stability while maintaining competitive accuracy.

2 Related Work

Graph Neural Networks. GNNs learn functions over graph structured data primarily through neighborhood aggregation and message passing, enabling topology- and attribute-aware representation learning [5, 6, 42, 46]. A complementary lens connects a

broad class of message-passing GNNs to localized polynomial filtering over a graph shift operator, which helps compare architectures through their effective smoothing and frequency preferences [10]. Prominent backbones include convolutional approximations [10, 26], attentional aggregation [50, 69, 71], scalable inductive frameworks [7, 18], deep residual networks [8, 28], and graph transformers for global dependency modeling [12, 64]. Despite these architectural variations, standard backbones typically execute a single fixed computation rule under frozen deployment, which locks in their test-time inductive bias (often reflected as a relatively fixed spectral preference) after training. When deployment conditions vary across environments and perturbations (e.g., degree distributions, homophily regimes, or noise types), this fixed bias cannot simultaneously preserve strong performance on the original graph, generalize under shift, and remain stable to perturbations, creating a fundamental tri-objective tension in frozen deployment scenarios.

Robust Graph Generalization. Research on robust Graph generalization has progressed along three intertwined threads: transferable pre-training, OOD generalization, and perturbation robustness, yet these lines are often developed with different objectives and evaluation protocols. Graph pre-training learns transferable representations through contrastive paradigms that encourage smoothness [19, 32, 36, 37, 51, 57, 58, 66, 76] or generative objectives that better preserve local structural details [9, 20, 48, 53, 54, 56]. However, pre-training typically serves as a static initialization, and downstream predictors still execute a fixed test-time computation rule, limiting adaptability when deployment conditions shift. OOD generalization methods address such shifts through invariant learning with test-time mechanisms [30, 52, 61, 75] or adaptive architectures with instance-conditional routing [34, 59, 60]. While instance-conditional routing expands mechanism coverage across various environments, existing designs often lack explicit deployment-time stability control (e.g., representation stabilization or sensitivity regularization), leaving them vulnerable to perturbations and noisy inputs. In parallel, perturbation-robust GNNs harden predictors through denoising, pruning, or smoothing under a fixed computation rule [14, 23, 27, 38, 72, 73], yet these static mechanisms can sacrifice expressivity needed under distribution shifts. Across these threads, methods typically optimize one or two objectives while treating the rest as auxiliary metrics. We propose STEM-GNN, which unifies instance-conditional computation with deployment-time stability control for robust graph generalization under frozen deployment.

3 Problem Formulation and Analysis

We formulate and analyze robust graph learning for deployed GNNs under frozen deployment through a tri-objective lens: **fit** (clean performance), **ood** (worst-environment generalization), and **stab** (perturbation robustness). The central question is how the *inference rule under frozen parameters* shapes these tradeoffs; we contrast static inference (\mathcal{H}_1) and instance-conditional computation (\mathcal{H}_2).

3.1 Problem Formulation

We study a graph neural network (GNN) $f_\theta : \mathcal{Z} \rightarrow \mathcal{U}$ under frozen deployment (no test-time updates). Input $z = (G, X)$ consists of an undirected graph $G = (V, E)$ and node features $X \in \mathbb{R}^{|V| \times d}$; the

GNN computes output $u = f_\theta(z)$ via message passing. Training uses distribution D_0 , while test environments E_{test} induce distributions $\{D_e\}$. Our deployment objective is captured by three risks: fitting on clean graphs, worst-environment OOD generalization, and inference-time stability. To model inference-time perturbations, we specify feature/structure discrepancy measures Δ_x, Δ_s together with budgets (ρ_x, ρ_s) . For input $z = (G, X)$, the admissible perturbation set is

$$B(z) := \{z' = (G', X') \mid \Delta_x(X', X) \leq \rho_x, \Delta_s(G', G) \leq \rho_s\}. \quad (1)$$

Let $\ell : \mathcal{U} \times \mathcal{Y} \rightarrow \mathbb{R}_+$ be the task loss and $d : \mathcal{U} \times \mathcal{U} \rightarrow \mathbb{R}_+$ an output discrepancy. We formalize the three risks as:

$$\mathcal{R}_{\text{fit}}(\theta) := \mathbb{E}_{(z,y) \sim D_0} [\ell(f_\theta(z), y)], \quad (2)$$

$$\mathcal{R}_{\text{ood}}(\theta) := \sup_{e \in E_{\text{test}}} \mathbb{E}_{(z,y) \sim D_e} [\ell(f_\theta(z), y)], \quad (3)$$

$$\mathcal{R}_{\text{stab}}(\theta) := \mathbb{E}_{(z,y) \sim D_0} \left[\sup_{z' \in B(z)} d(f_\theta(z), f_\theta(z')) \right]. \quad (4)$$

Analysis roadmap. Since the predictor is frozen, the tradeoff among these risks is shaped by the inference rule under fixed parameters. Hence, we contrast two paradigms: **(i) Static inference** (\mathcal{H}_1) applies a single message-passing rule to all inputs, yielding a stability-generalization tension (Sec. 3.2); **(ii) Instance-conditional computation** (\mathcal{H}_2) routes inputs through different computation paths, relaxing the \mathcal{H}_1 limitation but introducing routing instability under shifts and perturbations (Sec. 3.3). These insights inform STEM-GNN (Sec. 4).

3.2 \mathcal{H}_1 : Static Inference under a Stability Budget

Static inference deploys a *single frozen GNN computation rule* for all inputs: the same message-passing layers and readout are applied to every graph and node under fixed parameters. For GNNs, this creates a fundamental tension. To remain stable to feature/structure perturbations, the model must limit reliance on perturbation sensitive components (often associated with high-frequency, non-smooth signals on the graph), yet these same components can be crucial for fitting and worst-environment generalization. To isolate this GNN-specific tradeoff, we analyze a minimal witness family where a single scalar η_θ controls such reliance.

Static inference and a minimal witness family. Consider the witness family [44]:

$$f_\theta(G, X) := h_\theta(X_L + \eta_\theta X_H), \quad \eta_\theta \geq 0, \quad (5)$$

where X_L and X_H represent complementary *graph-induced spectral components* of node features, e.g., $X_L = P_L(G)X$ and $X_H = P_H(G)X$ for graph filters P_L, P_H that separate low-pass (smooth) and high-pass (non-smooth) information [10, 46]. The scalar reliance η_θ is fixed after training and shared across environments at deployment.

For prescribed $\alpha > 0$ and $\varepsilon \geq 0$, we define the slice-optimal worst-environment risk for \mathcal{H}_1 as:

$$\beta_1(\alpha, \varepsilon) := \inf_{\theta \in \mathcal{H}_1: \mathcal{R}_{\text{fit}}(\theta) \leq \alpha, \mathcal{R}_{\text{stab}}(\theta) \leq \varepsilon} \mathcal{R}_{\text{ood}}(\theta). \quad (6)$$

This worst-environment objective is standard in robust risk formulations under distribution shift [40].

Assumptions. Admissible perturbations mainly act on the high component [77], with magnitude at most ρ . The readout h_θ is L_h -Lipschitz [35] from the GNN embedding norm to the output metric. Good fitting (and at least one test environment) requires nontrivial reliance on the high component. Complete formal definitions and the proof are deferred to Appendix A.

We now show that a uniform stability budget induces an unavoidable constraint on η_θ , which in turn bounds worst-environment risk away from zero.

THEOREM 3.1 (WITNESS-FAMILY TENSION INDUCED BY A STABILITY BUDGET). *Under the assumptions, we define:*

$$\eta_{\max}(\varepsilon) := \frac{\varepsilon}{L_h \rho}, \quad \eta_{\min}(\alpha) := \inf \{\eta \geq 0 : \psi_{\text{fit}}(\eta) \leq \alpha\}. \quad (7)$$

Here $\psi_{\text{fit}}(\eta)$ is the monotone lower-bound function, relating the fitting risk to the reliance level η , and $e_1 \in E_{\text{test}}$ is the witness environment specified with its associated monotone lower bound $\psi_{e_1}(\eta)$. If $\eta_{\min}(\alpha) > \eta_{\max}(\varepsilon)$, then no GNN in (5) can satisfy both $\mathcal{R}_{\text{fit}}(\theta) \leq \alpha$ and $\mathcal{R}_{\text{stab}}(\theta) \leq \varepsilon$. Otherwise, for any θ in (5) satisfying $\mathcal{R}_{\text{fit}}(\theta) \leq \alpha$ and $\mathcal{R}_{\text{stab}}(\theta) \leq \varepsilon$, it holds that:

$$\mathcal{R}_{\text{ood}}(\theta) \geq \psi_{e_1}(\eta_{\max}(\varepsilon)) =: \underline{\beta}_1(\alpha, \varepsilon) > 0. \quad (8)$$

This result exposes a structural bottleneck for frozen GNN inference. The stability budget ε caps reliance at $\eta_\theta \leq \eta_{\max}(\varepsilon)$, because increasing reliance on X_H amplifies perturbation effects through the L_h -Lipschitz readout. Meanwhile, achieving fit risk at most α requires $\eta_\theta \geq \eta_{\min}(\alpha)$, since the high component carries task-relevant, graph-dependent information. When these constraints conflict ($\eta_{\min} > \eta_{\max}$), no predictor is feasible. When they are compatible, worst-environment risk is still bounded away from zero at $\underline{\beta}_1(\alpha, \varepsilon)$ (Eq. (8)). In other words, under a uniform constraint, static GNN inference cannot simultaneously achieve low fit, stability, and worst-environment risk.

3.3 \mathcal{H}_2 : Instance-Conditional Computation under Frozen Deployment

Section 3.2 revealed a fundamental bottleneck of static GNN inference under frozen deployment: when a *single frozen message-passing rule* must balance competing objectives across heterogeneous environments, all inputs share the same global reliance pattern, inducing an irreducible worst-environment floor under a uniform stability budget. This is not an artifact of the witness family; it reflects the rigidity of applying one computation rule everywhere. Instance-conditional computation (ICC) relaxes this rigidity by routing inputs to different *effective message-passing mechanisms*, expanding the mechanism family available at deployment. However, ICC also introduces a new fragility pathway: routing decisions can drift under distribution shifts and admissible perturbations, compounding downstream errors. This subsection formalizes ICC and isolates the levers governing OOD risk and stability.

ICC class. We define the ICC (instance-conditional computation) [2] class of a GNN f_θ under frozen deployment. Formally, there exist a routing space \mathcal{R} , a routing map $r_\theta : \mathcal{Z} \rightarrow \mathcal{R}$, and an execution map $F : \mathcal{R} \times \mathcal{Z} \rightarrow \mathcal{U}$, such that:

$$f_\theta(z) := F(r_\theta(z), z), \quad z = (G, X). \quad (9)$$

Here r_θ selects an input-dependent routed state (e.g., a conditional path/state selector), and F executes the corresponding routed GNN computation (e.g., path-conditioned message passing [39]).

Why this helps in a GNN context. Unlike static inference, ICC varies $r_\theta(z)$ across inputs, enabling different effective message-passing behaviors (analogous to varying reliance in \mathcal{H}_1) without changing parameters, thus improving coverage over heterogeneous environments. The tradeoff is a new stability pathway: under distribution shifts and admissible feature/structure perturbations (per $B(z)$), routing can drift and degrade robustness [13]. We define the slice-optimal worst-environment risk for \mathcal{H}_2 as:

$$\beta_2(\alpha, \varepsilon) := \inf_{\theta \in \mathcal{H}_2: \mathcal{R}_{\text{fit}}(\theta) \leq \alpha, \mathcal{R}_{\text{stab}}(\theta) \leq \varepsilon} \mathcal{R}_{\text{ood}}(\theta). \quad (10)$$

Handle 1: OOD risk via coverage and selection. *Question: how can ICC reduce worst-environment risk?* Consider an ICC instantiation where execution selects from a finite family of mechanisms (routed states) [22]. Let β_{cov} denote worst-environment *coverage* (for each environment, the best achievable loss within the family), and $\delta_{\text{sel}}(e)$ denotes *selection error* in environment e (probability of selecting a non-oracle state). Assume the evaluation loss is bounded by L_{\max} on test environments (used only for analysis). Then worst-environment risk is controlled by coverage and selection:

$$\mathcal{R}_{\text{ood}}(\theta) \leq \beta_{\text{cov}} + L_{\max} \cdot \sup_{e \in E_{\text{test}}} \delta_{\text{sel}}(e). \quad (11)$$

What this exposes. Eq. (11) isolates two levers: (i) expand the mechanism family to reduce β_{cov} , and (ii) make routing reliable under shift to reduce $\sup_e \delta_{\text{sel}}(e)$. In a GNN, (i) can be achieved by diverse message-passing experts under a shared budget (e.g., an MoE encoder), while (ii) depends on stable routing signals and representations. The formal definitions and proof are provided in Appendix B.

Handle 2: stability via routing decomposition. *Question: how does ICC change stability under admissible perturbations?* Stability now depends on both execution sensitivity under a fixed routed state and routing drift. Let $\mathcal{R}_{\text{base}}(\theta)$ denote routing-fixed execution sensitivity (output change under admissible perturbations when the routed state is held fixed), and let $\mathcal{R}_{\text{route}}(\theta)$ denote routing drift (change in the routed state). Let $L_F^B(D_0)$ denote an execution envelope converting routing changes into output changes, uniformly over admissible perturbations to reference inputs [25]. Then:

$$\mathcal{R}_{\text{stab}}(\theta) \leq \mathcal{R}_{\text{base}}(\theta) + L_F^B(D_0) \cdot \mathcal{R}_{\text{route}}(\theta). \quad (12)$$

What this exposes. Eq. (12) highlights three stability targets: reduce routing-fixed sensitivity $\mathcal{R}_{\text{base}}$ (as in static models), reduce routing drift $\mathcal{R}_{\text{route}}$ (absent in \mathcal{H}_1), and bound amplification $L_F^B(D_0)$ (how strongly execution magnifies routing changes). In a GNN, routing drift can be mitigated by stabilizing/discretizing the routing interface (e.g., tokenized representations), while amplification can be controlled via regularization (e.g., Lipschitz constraints on the readout). The formal definitions and proof are provided in Appendix B.

Takeaway. Contrasting \mathcal{H}_1 and \mathcal{H}_2 clarifies both the promise and the design requirements of ICC. While \mathcal{H}_1 can face an irreducible worst-environment floor under a uniform stability budget (Eq. (8)), ICC can reduce OOD risk by improving coverage and selection (Eq. (11)), and can improve stability by jointly controlling routing drift and execution amplification (Eq. (12)). Guided by these levers,

STEM-GNN instantiates robust ICC via three components: an MoE encoder for coverage expansion (addressing β_{cov}), VQ tokenization for routing stabilization (reducing $\mathcal{R}_{\text{route}}$), and Lipschitz regularization for amplification control (reducing $L_F^B(D_0)$).

4 Methodology

With theoretical findings, we propose **STEM-GNN**, a pretrain-then-finetune GNN framework for robust instance-conditional inference under frozen deployment (Figure 2). Specifically, an MoE encoder first routes instances to input-dependent expert combinations, expanding mechanism coverage across heterogeneous deployment scenarios. The resulting intermediate representations are then passed through a vector-quantized token interface that maps them to a fixed codebook, so the prediction head consumes tokens rather than drifting embeddings. Finally, Lipschitz regularization on the head further bounds amplification of residual changes, including token switches, yielding controlled and robust outputs end-to-end.

4.1 Coverage Expansion via MoE Encoder

Static inference applies a single computation rule to all inputs, which can be overly restrictive under heterogeneous deployment conditions. We therefore use a MoE message-passing encoder to expand the deployed mechanism family under a fixed parameter and compute budget, with globally shared frozen experts and input-dependent routing that can vary across nodes and layers.

MoE message passing with soft routing. Let $h_v^{(l)} \in \mathbb{R}^{d_l}$ denote the representation of node v at layer l . Each MoE layer maintains K shared expert operators $\{f_k^{(l)}\}_{k=1}^K$ and a lightweight router $g^{(l)}$. The router outputs a soft routing distribution:

$$\pi^{(l)}(v) = \text{softmax}(g^{(l)}(h_v^{(l)})) \in \Delta^{K-1}, \quad (13)$$

where Δ^{K-1} is the probability simplex over K experts. Each layer first computes a neighborhood summary:

$$z_v^{(l)} = \psi^{(l)}\left(h_v^{(l)}, \text{AGG}_{u \in \mathcal{N}(v)} \phi^{(l)}(h_u^{(l)})\right), \quad (14)$$

then updates the representation via a soft mixture of expert transforms:

$$h_v^{(l+1)} = \sigma\left(\sum_{k=1}^K \pi_k^{(l)}(v) f_k^{(l)}(z_v^{(l)})\right), \quad (15)$$

where σ is a pointwise nonlinearity. During training, routing is optimized with a Gumbel-Softmax relaxation (temperature $\tau > 0$); deployment uses the deterministic softmax in Eq. (13).

Effective mechanisms and coverage. Eq. (15) realizes an input-dependent effective operator:

$$f_{\text{eff}}^{(l)}(\cdot; v) := \sum_{k=1}^K \pi_k^{(l)}(v) f_k^{(l)}(\cdot), \quad (16)$$

so a single frozen parameter set realizes a family of mechanisms indexed by the routing distributions $\{\pi^{(l)}(v)\}$. This enlarges the deployed mechanism family under a fixed budget, improving coverage across diverse deployment scenarios.

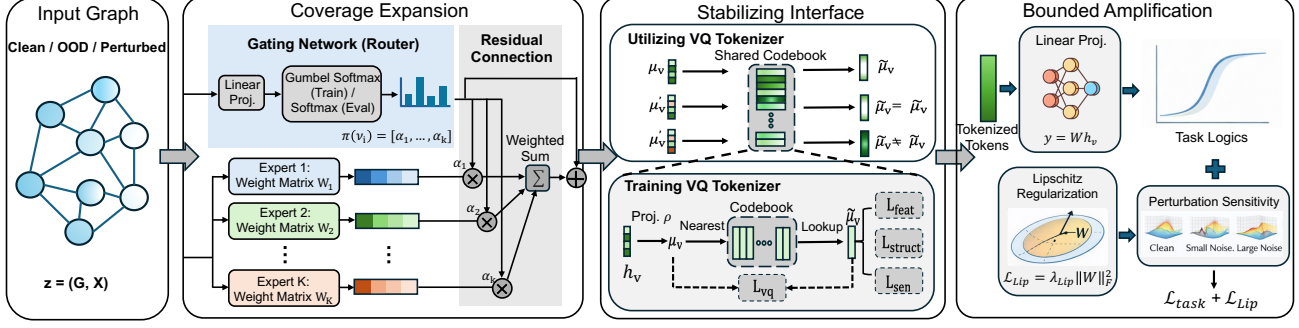


Figure 2: The STEM-GNN framework: the MoE message-passing encoder first expands mechanism coverage via input-dependent routing, then a VQ token interface discretizes intermediate representations with a shared codebook to stabilize the encoder-to-head pathway, and finally a Lipschitz-regularized prediction head bounds amplification of residual variations.

4.2 Stabilizing Intermediate Representations via VQ Tokenization

MoE enables input-dependent execution, but the encoder outputs can still drift under environment shifts and admissible perturbations. Under frozen deployment, this drift directly perturbs the input to the task head. To stabilize the encoder-to-head interface, a vector-quantized (VQ) token layer discretizes intermediate representations so the head consumes tokens from a fixed codebook rather than drifting continuous embeddings.

Specifically, let $h_v \in \mathbb{R}^d$ be the encoder output for node $v \in V$, and let $u_v = \rho(h_v) \in \mathbb{R}^{d_q}$ be a projected embedding. Given a codebook $C = \{c_j\}_{j=1}^M \subset \mathbb{R}^{d_q}$, VQ assigns a token index and codeword by nearest-code matching:

$$q_\theta(v; z) := \arg \min_{1 \leq j \leq M} \|u_v(z) - c_j\|_2, \quad Q(u_v(z)) := c_{q_\theta(v; z)}. \quad (17)$$

The projection ρ and codebook C are learned with the standard VQ-VAE objective [49]:

$$\mathcal{L}_{\text{vq}} = \mathbb{E}_v \left[\|\text{sg}(u_v) - Q(u_v)\|_2^2 + \beta \|u_v - \text{sg}(Q(u_v))\|_2^2 \right], \quad (18)$$

where $\text{sg}(\cdot)$ denotes stop-gradient. During pretraining, we train the encoder, ρ , and C jointly, and apply our feature-level, structure-level, and semantic-level pretraining signals on the tokenized representations. During finetuning, we freeze the codebook C and the quantization rule in Eq. (17) to preserve a consistent interface partition. The deployed predictor is:

$$f_\theta(z) := g(Q(u_\theta(z))), \quad (19)$$

where g is the task head operating on tokenized embeddings.

Token invariance under small perturbations. For each node v , define the quantization margin at z :

$$m_v(z) := \min_{j \neq q_\theta(v; z)} \|u_v(z) - c_j\|_2 - \|u_v(z) - c_{q_\theta(v; z)}\|_2. \quad (20)$$

LEMMA 4.1 (MARGIN-BASED INVARIANCE OF THE VQ INTERFACE). If for every $v \in V$,

$$\sup_{z' \in B(z)} \|u_v(z') - u_v(z)\|_2 < \frac{1}{2} m_v(z), \quad (21)$$

then $q_\theta(v; z') = q_\theta(v; z)$ for all $z' \in B(z)$ and $v \in V$, and thus $Q(u_\theta(z')) = Q(u_\theta(z))$ for all $z' \in B(z)$.

PROOF. The detailed proof is provided in Appendix C.1. \square

4.3 Bounding Output Amplification via Lipschitz Regularization

VQ stabilizes the encoder-head interface by mapping representations to a fixed codebook. However, when perturbations cause token switches, the remaining deployment variation depends on how strongly the task head amplifies its input changes. We thus regularize the head to bound its Lipschitz constant [35], constraining input-output amplification under shifts and perturbations.

Specifically, let $r(z) \in \mathbb{R}^{d_q}$ denote the input after tokenization (nodewise for node tasks, or after a pooling for graph tasks), and define $f_\theta(z) = f_t(r(z))$. In our implementation, the head is linear:

$$f_t(r) = Wr + b. \quad (22)$$

Its Lipschitz constant under $\|\cdot\|_2$ equals $\|W\|_2$ and satisfies $\|W\|_2 \leq \|W\|_F$. To softly control this constant during training, we add a Frobenius penalty:

$$\mathcal{L} = \mathcal{L}_{\text{task}} + \lambda_{\text{lip}} \|W\|_F^2, \quad (23)$$

which discourages large operator norms and reduces worst-case amplification through the head.

Let C be the VQ codebook and $\text{diam}(C) = \max_{i,j} \|c_i - c_j\|_2$. Since VQ restricts head inputs to come from a finite set of token embeddings, any token switch induces a bounded change in the head input (bounded by the codebook diameter, up to pooling for graph-level tasks). With a controlled head Lipschitz constant, the resulting output change is bounded accordingly.

PROPOSITION 4.2 (BOUNDED OUTPUT AMPLIFICATION UNDER TOKEN SWITCHES). Assume the head f_t is L -Lipschitz under $\|\cdot\|_2$. Then for any admissible perturbation $z' \in B(z)$, the output satisfies

$$\|f_t(r(z')) - f_t(r(z))\|_2 \leq L \cdot \text{diam}(C), \quad (24)$$

PROOF. The detailed proof is provided in Appendix C.2. \square

Tokenization bounds how much the head input can change when tokens switch, while Lipschitz regularization limits how much any such input change can be amplified into output variation. Together, they control deployment-time sensitivity without changing inference-time computation.

Table 1: Clean graph results on node, link, and graph tasks. Node/Link/Graph metrics are accuracy (%); link prediction is multi-class relation classification (predicting relation type r given an entity pair (h, t)). Best per column is **bold**, second best is underlined. Results are reported as mean \pm std over k runs with different random seeds ($k = 10$ by default, $k = 20$ on *WikiCS*).

Method	Node Classification				Link Classification		Graph Classification		
	Cora	PubMed	Wiki-CS	Arxiv	WN18RR	FB15K237	HIV	PCBA	Avg.
Linear	58.03 \pm 2.33	68.66 \pm 2.24	70.36 \pm 0.58	66.50 \pm 0.14	78.50 \pm 0.59	87.39 \pm 0.07	66.37 \pm 1.11	72.30 \pm 0.34	71.01
GCN[26]	75.65 \pm 1.37	75.61 \pm 2.10	75.28 \pm 1.34	<u>71.40</u> \pm 0.08	73.79 \pm 0.39	82.22 \pm 0.28	64.84 \pm 4.78	71.32 \pm 0.49	73.76
GAT[50]	76.24 \pm 1.62	74.86 \pm 1.87	76.78 \pm 0.78	70.87 \pm 0.24	80.16 \pm 0.27	88.93 \pm 0.15	65.54 \pm 6.93	70.12 \pm 0.89	75.44
GIN[63]	73.59 \pm 2.10	69.51 \pm 6.87	49.77 \pm 4.72	65.05 \pm 0.50	74.02 \pm 0.55	83.21 \pm 0.53	66.86 \pm 3.48	72.69 \pm 0.22	69.34
DGI[51]	72.10 \pm 0.34	73.13 \pm 0.64	75.32 \pm 0.95	69.15 \pm 0.20	75.75 \pm 0.90	81.34 \pm 0.15	59.62 \pm 1.21	63.31 \pm 0.89	71.22
BGRL[47]	71.20 \pm 0.30	75.29 \pm 1.33	76.53 \pm 0.69	71.19 \pm 0.20	75.44 \pm 0.30	80.66 \pm 0.29	63.95 \pm 1.06	67.09 \pm 1.00	72.67
GraphMAE[20]	73.10 \pm 0.40	74.32 \pm 0.33	77.61 \pm 0.39	70.90 \pm 0.31	78.99 \pm 0.48	85.30 \pm 0.16	61.04 \pm 0.55	63.30 \pm 0.78	73.07
GIANT[9]	75.13 \pm 0.49	72.31 \pm 0.53	76.56 \pm 0.88	70.10 \pm 0.32	84.36 \pm 0.30	87.45 \pm 0.54	65.44 \pm 1.39	61.49 \pm 0.99	74.11
GFT[53]	77.83 \pm 1.17	<u>77.70</u> \pm 1.39	78.40 \pm 0.70	69.17 \pm 0.57	<u>91.19</u> \pm 0.33	<u>89.91</u> \pm 0.05	70.93 \pm 1.02	<u>78.95</u> \pm 0.27	<u>79.26</u>
CaNet[59]	76.41 \pm 1.48	75.33 \pm 1.54	<u>78.88</u> \pm 0.45	66.70 \pm 0.32	–	–	–	–	–
GraphMETRO[60]	75.69 \pm 3.34	75.24 \pm 1.68	74.59 \pm 2.08	<u>67.27</u> \pm 0.35	–	–	–	–	–
MARIO[75]	<u>77.85</u> \pm 1.31	77.12 \pm 0.98	78.60 \pm 0.44	67.57 \pm 0.45	–	–	–	–	–
TFEGNN[11]	77.33 \pm 1.47	77.04 \pm 1.02	76.74 \pm 0.64	68.56 \pm 0.67	–	–	–	–	–
STEM-GNN	79.53 \pm 1.32	77.84 \pm 1.66	80.11 \pm 0.53	72.31 \pm 0.25	92.34 \pm 0.25	90.26 \pm 0.16	73.54 \pm 1.02	80.39 \pm 0.38	80.79

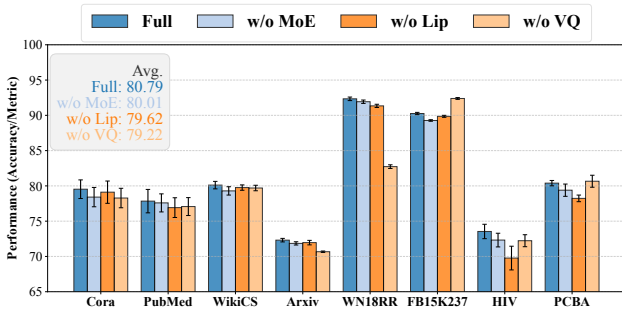


Figure 3: Ablation study on clean original graphs (mean \pm std). We compare the full STEM-GNN with variants removing MoE (w/o MoE), Lipschitz regularization (w/o Lip), or VQ (w/o VQ) across all benchmarks, and report the average performance across datasets.

5 Experiments

5.1 Experimental Setup

Datasets. We evaluate on nine datasets spanning node, link, and graph tasks across diverse domains: (i) citation networks (Cora, PubMed, and Arxiv) and a Wikipedia graph (WikiCS) for node classification; (ii) knowledge graphs (WN18RR and FB15K-237) for link-level multi-class relation prediction; (iii) molecular graphs (HIV, PCBA, and ChEMBL) for graph classification. Dataset statistics and preprocessing details are reported in Appendix D.1.

Baselines. We compare STEM-GNN with various baselines from three families: (i) supervised baselines: Linear, GCN [26], GAT [50], and GIN [63]; (ii) self/weakly-supervised pretraining and foundation methods: DGI [51], BGRL [47], GraphMAE [20], GIANT [9],

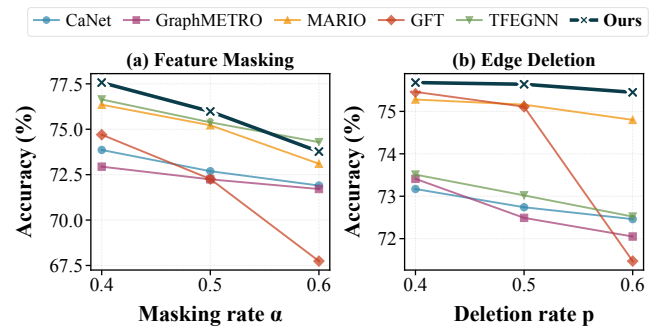


Figure 4: Stability under inference-time perturbation on two node benchmarks. Left: Cora. Right: PubMed. In each dataset, (a) shows feature masking with masking rate α , and (b) shows structural corruption via edge deletion with deletion rate p .

and GFT [53]; (iii) OOD- and robustness-oriented methods: CaNet [59], GraphMETRO [60], MARIO [75], and TFEGLNN [11].

Implementation Details. Across all experiments, models are trained on clean graphs and evaluated under frozen deployment, with no test-time updates or adaptation. For baselines, we follow the authors' recommended setup (official code when available) and run all methods under a matched protocol (details in Appendix D); we then evaluate models under three conditions: (i) clean performance on the corresponding test split, (ii) stability under inference-time perturbations (feature masking and edge deletion at varying levels), and (iii) generalization under distribution shifts defined by held-out OOD tail splits (degree- and homophily-based). Results are averaged over 10 random seeds to reduce randomness impact.

5.2 Results on Clean Graphs

Main Results. Table 1 reports clean-graph performance across node, link, and graph tasks. Ours achieves the best average (80.79%),

Table 2: Node classification accuracy (%) under attribute-defined distribution shifts. Degree shift and homophily shift evaluate models trained/selected on the original split and tested on buckets defined by the corresponding attribute. OOD-low/OOD-high denote the bottom/top 15% test nodes by the shift attribute.

Dataset	Bucket	CaNet[59]	GraphMETRO[60]	MARIO[75]	GFT[53]	TFEGNN[11]	STEM-GNN
Cora	ID	84.12 \pm 1.54	83.78 \pm 1.19	87.07 \pm 1.81	87.01 \pm 1.48	86.63 \pm 1.45	87.39 \pm 1.14
	OOD-low	76.35 \pm 1.63	77.00 \pm 1.65	78.77 \pm 1.03	81.22 \pm 0.70	83.00 \pm 0.82	82.73 \pm 0.85
	OOD-high	84.38 \pm 0.83	82.22 \pm 2.99	85.71 \pm 0.71	84.98 \pm 1.11	85.71 \pm 1.79	86.08 \pm 1.02
PubMed	ID	89.07 \pm 0.48	87.93 \pm 0.42	84.97 \pm 0.68	89.29 \pm 0.53	89.65 \pm 0.47	90.61 \pm 0.35
	OOD-low	88.85 \pm 0.14	87.15 \pm 0.22	83.50 \pm 0.52	88.73 \pm 0.46	89.14 \pm 0.59	89.44 \pm 0.42
	OOD-high	88.75 \pm 0.49	88.26 \pm 0.31	85.86 \pm 0.33	88.95 \pm 0.39	86.38 \pm 0.48	89.95 \pm 0.22
WikiCS	ID	83.48 \pm 0.63	83.67 \pm 1.41	85.56 \pm 0.83	85.07 \pm 0.53	81.55 \pm 0.97	86.03 \pm 0.49
	OOD-low	75.68 \pm 0.45	75.99 \pm 1.53	74.64 \pm 0.95	76.01 \pm 1.12	78.81 \pm 0.69	77.26 \pm 0.77
	OOD-high	86.17 \pm 0.53	81.38 \pm 2.45	83.45 \pm 0.76	85.80 \pm 0.74	85.18 \pm 0.87	86.23 \pm 1.56
Avg		84.09	83.04	83.28	85.23	85.12	86.19
Cora	ID	83.97 \pm 0.64	84.52 \pm 1.68	85.65 \pm 1.21	87.20 \pm 1.90	86.11 \pm 1.20	87.56 \pm 1.23
	OOD-low	79.41 \pm 1.16	78.08 \pm 1.63	81.48 \pm 0.96	77.83 \pm 0.86	81.53 \pm 1.65	80.12 \pm 1.13
	OOD-high	85.52 \pm 1.60	84.81 \pm 1.57	87.44 \pm 1.66	90.44 \pm 0.93	88.28 \pm 0.89	91.03 \pm 0.81
PubMed	ID	88.15 \pm 0.27	87.38 \pm 0.51	87.55 \pm 0.42	89.70 \pm 0.58	89.08 \pm 0.41	90.49 \pm 0.43
	OOD-low	85.19 \pm 0.34	84.90 \pm 0.52	82.24 \pm 0.23	85.52 \pm 0.45	87.34 \pm 0.54	86.26 \pm 0.43
	OOD-high	87.08 \pm 0.20	86.04 \pm 0.61	85.86 \pm 0.69	92.41 \pm 0.33	88.25 \pm 0.28	92.85 \pm 0.39
WikiCS	ID	83.72 \pm 0.49	85.39 \pm 0.73	83.57 \pm 0.44	84.64 \pm 0.60	83.60 \pm 0.60	85.77 \pm 0.53
	OOD-low	81.60 \pm 0.48	82.39 \pm 0.71	80.31 \pm 0.61	80.08 \pm 0.61	81.55 \pm 0.63	80.87 \pm 0.40
	OOD-high	83.36 \pm 0.44	87.95 \pm 0.53	85.47 \pm 0.25	89.42 \pm 0.52	85.59 \pm 0.40	89.88 \pm 0.54
Avg		84.22	84.61	84.40	86.36	85.70	87.20

ranking first or second on 7 out of 8 benchmarks, showing that clean accuracy remains compatible with deployment-oriented design under frozen deployment. Among pretrain-then-finetune baselines (e.g., DGI, GraphMAE), Ours attains the best overall Avg. and is top-ranked on most datasets. Compared to GFT (79.26%), Ours improves most on node (+1.70 Cora, +1.91 Arxiv) and graph tasks (+2.61 HIV, +1.44 PCBA), while remaining competitive on link tasks (+1.15 WN18RR, +0.35 FB15K237). This pattern suggests an advantage on higher-heterogeneity settings (node/graph), where a single fixed computation is more likely to be suboptimal across instances. We also observe smaller standard deviations on several datasets (e.g., \pm 0.25 vs. \pm 0.57 on Arxiv), indicating reduced sensitivity to random seeds. Against OOD/robustness-oriented baselines on the shared node benchmarks, Ours remains competitive while also delivering strong link and graph performance within the same protocol. The following sections show that the same frozen model translates these gains to distribution shifts and perturbations.

Ablation Study. Figure 3 shows that the full model achieves the best average on clean graphs (80.79%), and each ablation lowers the average (w/o MoE: 80.01%, w/o Lip: 79.62%, w/o VQ: 79.22%), indicating non-redundant benefits (Appendix D, Table 6). Among them, MoE yields the most uniform improvements across node/link/graph benchmarks, while VQ and Lipschitz regularization are more task-dependent, with larger gains on higher-heterogeneity or pooled graph settings, consistent with stabilizing the interface and controlling amplification. Notably, the full model avoids sharp, dataset-specific regressions seen in some ablations, suggesting that the components complement each other by trading off coverage (MoE) against sensitivity control (VQ+Lip) rather than providing interchangeable capacity. This complementarity helps explain why gains

are broad across tasks: the same pretrain-then-finetune pipeline remains strong on clean data while retaining headroom for robustness under shifts and perturbations evaluated next.

5.3 Results on Noisy Graphs

We train on clean graphs and use clean validation for model selection, then evaluate the same frozen model under inference-time perturbations: (a) feature masking ($\alpha \in \{0.4, 0.5, 0.6\}$) and (b) edge deletion ($p \in \{0.4, 0.5, 0.6\}$). Figure 4 shows that Ours degrades most gracefully and maintains the strongest accuracy trend across both corruption types. Notably, the margin widens at higher severities, where several baselines exhibit sharper drops, suggesting improved resilience to partial attribute loss and connectivity disruption without noise-aware training. This behavior is consistent with VQ stabilizing the encoder-to-head interface under small perturbations (Lemma 4.1) and Lipschitz control limiting amplification when token switches occur (Proposition 4.2). Complete results are in Appendix D.

5.4 Out-Of-Distribution Generalization

We evaluate OOD generalization by training on the clean original split and using original validation accuracy for model selection only; the same frozen model is then tested on attribute-defined distribution shifts. Table 2 reports results under degree shift and homophily shift, where OOD-low/OOD-high denote the bottom/top 15% by the respective attribute. Ours achieves the best average under both shifts (86.19% degree, 87.20% homophily), with the gains concentrating on challenging OOD-high buckets, e.g., degree OOD-high on Cora (86.08 vs. GFT's 84.98) and homophily OOD-high on Cora (91.03 vs. GFT's 90.44). This trend is consistent with stronger benefits when neighborhood aggregation is more influential, where

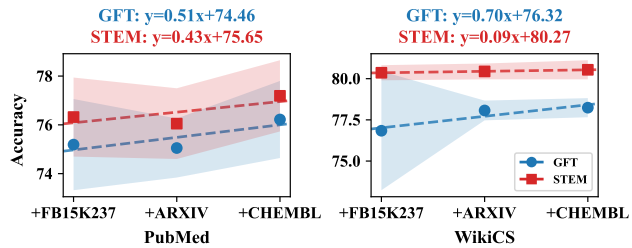


Figure 5: Cross-domain transfer with increasing pre-training diversity. STEM-GNN is less sensitive to the source mixture than GFT on PubMed and WikiCS (least-squares fits shown).

Table 3: Tri-objective results. We select the epoch by clean validation, evaluate the frozen checkpoint on Fit, OOD-worst, and Perturb-mean (feature masking). Avg is their mean.

Dataset	Method	Fit↑	OOD-worst↑	Perturb-mean↑	Avg↑
Cora	CaNet [59]	83.63±1.86	75.20±1.80	82.53±1.76	80.45±1.81
	GraphMETRO [60]	83.67±1.46	79.11±1.14	82.95±1.43	81.91±1.34
	MARIO [75]	83.39±1.61	78.45±1.83	83.11±1.49	81.59±1.64
	GFT [53]	86.58±1.75	76.47±1.59	84.14±2.34	82.40±1.89
	TFEGNN [11]	83.77±0.98	77.07±1.65	83.57±1.20	81.47±1.28
	Ours	87.31±1.56	78.45±0.77	85.88±1.38	83.88±1.24
PubMed	CaNet [59]	88.43±0.42	85.88±0.44	86.08±0.21	86.80±0.36
	GraphMETRO [60]	87.63±0.70	84.30±0.49	83.36±0.97	85.10±0.72
	MARIO [75]	86.14±0.56	84.13±0.57	83.55±0.63	84.61±0.59
	GFT [53]	89.49±0.65	84.60±0.39	84.68±1.77	86.26±0.94
	TFEGNN [11]	88.52±0.65	85.12±0.57	86.50±0.32	86.71±0.51
	Ours	90.14±0.62	84.77±0.50	86.26±0.66	87.06±0.59
WikiCS	CaNet [59]	83.13±0.98	79.86±0.43	81.09±0.86	81.36±0.76
	GraphMETRO [60]	81.77±1.46	76.94±1.23	78.53±1.28	79.08±1.32
	MARIO [75]	83.25±0.86	77.28±0.93	81.21±0.89	80.58±0.89
	GFT [53]	85.41±0.96	78.46±0.79	82.44±1.12	82.10±0.96
	TFEGNN [11]	83.91±0.32	80.84±0.53	82.21±0.28	82.32±0.38
	STEM-GNN	85.57±0.76	79.02±0.67	83.90±0.69	82.83±0.71

stable routing and a discretized interface help mitigate shift-induced variation. Overall, the results align with Eq. 11: improved worst-environment risk through both coverage expansion (β_{cov}) and stable selection (smaller δ_{sel}).

5.5 Transferability Analysis

Figure 5 evaluates cross-domain transfer by increasing pre-training diversity ($\text{FB15K-237} \rightarrow +\text{Arxiv} \rightarrow +\text{ChEMBL}$) and fine-tuning on PubMed and WikiCS. Beyond mean accuracy, STEM-GNN shows stronger *mixture robustness*: it is less sensitive to the source mixture and exhibits flatter scaling than GFT (least-squares slopes: PubMed 0.43 vs. 0.51; WikiCS 0.09 vs. 0.70). Thus, adding heterogeneous sources yields more predictable gains for STEM-GNN, while GFT shows larger composition-induced variability, especially on WikiCS. This is valuable under frozen deployment, where practitioners must commit to a fixed pre-training recipe without exhaustive tuning. The pattern aligns with MoE expanding coverage across heterogeneous sources and Lipschitz control limiting amplification of source-induced shifts, reducing negative transfer when mixing disparate domains.

5.6 Tri-Objective results

Main Results. Table 3 reports a unified tri-objective evaluation on three node benchmarks. Each method is trained once, selected by clean validation accuracy, then evaluated on: (i) *Fit* (clean test

Table 4: Tri-objective ablation on node benchmarks. We report *Fit*, *OOD-worst*, *Perturb-mean*, and *Avg*.

Dataset	Metric	Full	w/o MoE	w/o VQ	w/o Lip
Cora	Fit	87.31±1.56	86.73±1.32	86.57±1.44	87.78±1.39
	OOD-worst	78.45±0.77	77.76±1.66	77.01±1.34	78.25±1.10
	Perturb-mean	85.88±1.38	85.04±1.47	85.37±1.46	85.33±1.22
PubMed	Fit	90.14±0.62	89.07±0.55	89.26±0.35	89.30±0.58
	OOD-worst	84.77±0.50	84.14±0.35	84.09±0.47	83.58±0.49
	Perturb-mean	86.26±0.66	85.68±0.71	85.12±0.96	85.37±0.60
WikiCS	Fit	85.57±0.76	85.30±0.56	84.96±0.57	85.40±0.55
	OOD-worst	79.02±0.67	77.43±0.54	78.30±0.53	77.99±0.50
	Perturb-mean	83.90±0.69	82.03±0.99	83.16±0.59	82.59±0.68
Avg.		84.59	83.69	83.76	83.95

accuracy), (ii) *OOD-worst* (minimum accuracy over homophily-shifted splits), and (iii) *Perturb-mean* (mean accuracy under feature masking, $\alpha \in \{0.2, 0.4, 0.6, 0.8\}$), with Avg averaging the three. Ours achieves the best Avg on all datasets (Cora: 83.88, PubMed: 87.06, WikiCS: 82.83), indicating a better balance under frozen deployment. Crucially, the gain comes from improving *Fit* and *Perturb-mean* while also improving *OOD-worst*, rather than trading objectives. On Cora, Ours improves over GFT on all three axes (*Fit* 87.31 vs. 86.58, *Perturb-mean* 85.88 vs. 84.14, *OOD-worst* 78.45 vs. 76.47), yielding +1.48 in Avg and visibly tightening the tri-objective frontier. More broadly, under the same clean-only selection criterion, lifting one axis often fails to lift the others, revealing tri-objective tension within a single protocol. This suggests that coverage expansion and stability control remain compatible with clean generalization, consistent with §3.3.

Ablation Study. Table 4 shows the strongest complementarity in the tri-objective setting: the full model achieves the best Avg (84.59), and no ablation improves *OOD-worst* and *Perturb-mean* simultaneously. Removing MoE causes the most consistent robustness drop across datasets (e.g., WikiCS *OOD-worst* 79.02→77.43; PubMed *Perturb-mean* 86.26→85.68), supporting MoE as the main driver of mechanism coverage under heterogeneous test conditions. VQ primarily stabilizes robustness: w/o VQ often keeps *Fit* similar but reduces *OOD-worst*/*Perturb-mean* overall (e.g., Cora *OOD-worst* 78.45→77.01; PubMed *Perturb-mean* 86.26→85.12), showing that a discrete interface suppresses drift. Lipschitz shows fit-robustness tradeoff: w/o Lip can raise *Fit* (Cora 87.31→87.78) but lowers *OOD-worst*/*Perturb-mean* (Cora 78.45→78.25, 85.88→85.33), yielding a worse Avg (84.59→83.95). Overall, MoE expands coverage under shift, VQ stabilizes the encoder-head interface under drift, and Lipschitz control limits amplification under perturbations.

6 Conclusion

We show that the test-time computation mechanism - not the training objective alone - governs the tri-objective balance in frozen graph deployment. Our analysis explains why static inference hits a structural floor and how instance-conditional computation adds leverage but introduces routing failure modes. STEM-GNN addresses these levers via MoE routing, VQ tokenization, and Lipschitz control; ablations confirm complementarity across nine benchmarks. Under clean-only selection with OOD and perturbation evaluation, STEM-GNN achieves a better balance through MoE coverage and VQ+Lip stability control in practice. This shows that

expanding mechanisms and constraining sensitivity can coexist in a single frozen model. However, fixed expert count and a frozen codebook may limit adaptability to distant domains. Adaptive expert allocation, online codebook refinement, and temporal drift are promising future research directions.

References

- [1] Peter W Battaglia, Jessica B Hamrick, Victor Bapst, Alvaro Sanchez-Gonzalez, Vinicius Zambaldi, Mateusz Malinowski, Andrea Tacchetti, David Raposo, Adam Santoro, Ryan Faulkner, et al. 2018. Relational inductive biases, deep learning, and graph networks. *arXiv* (2018).
- [2] Emmanuel Bengio, Pierre-Luc Bacon, Joelle Pineau, and Doina Precup. 2015. Conditional computation in neural networks for faster models. *arXiv* (2015).
- [3] Fedor Borisyuk, Shihai He, Yunbo Ouyang, Morteza Ramezani, Peng Du, Xiaochen Hou, Chengming Jiang, Nitin Pasumarthy, Priya Bannur, Birjodh Tiwana, et al. 2024. Lignn: Graph neural networks at linkedin. In *KDD*.
- [4] Michael M Bronstein, Joan Bruna, Taco Cohen, and Petar Veličković. 2021. Geometric deep learning: Grids, groups, graphs, geodesics, and gauges. *arXiv* (2021).
- [5] Michael M Bronstein, Joan Bruna, Yann LeCun, Arthur Szlam, and Pierre Vandergheynst. 2017. Geometric deep learning: going beyond euclidean data. *IEEE Signal Processing Magazine* (2017).
- [6] Joan Bruna. 2013. Spectral networks and locally connected networks on graphs. *arXiv* (2013).
- [7] Jie Chen, Tengfei Ma, and Cao Xiao. 2018. Fastgcn: fast learning with graph convolutional networks via importance sampling. *arXiv* (2018).
- [8] Ming Chen, Zhenwei Wei, Zengfeng Huang, Bolin Ding, and Yaliang Li. 2020. Simple and deep graph convolutional networks. In *ICML*.
- [9] Eli Chien, Wei-Cheng Chang, Cho-Jui Hsieh, Hsiang-Fu Yu, Jiong Zhang, Olgica Milenkovic, and Inderjit S Dhillon. 2021. Node feature extraction by self-supervised multi-scale neighborhood prediction. *arXiv* (2021).
- [10] Michaël Defferrard, Xavier Bresson, and Pierre Vandergheynst. 2016. Convolutional neural networks on graphs with fast localized spectral filtering. *NeurIPS* (2016).
- [11] Rui Duan, Mingjian Guang, Junli Wang, Chungang Yan, Hongda Qi, Wenkang Su, Can Tian, and Haoran Yang. 2024. Unifying homophily and heterophily for spectral graph neural networks via triple filter ensembles. *Proceedings of the ACM Web Conference* (2024).
- [12] Vijay Prakash Dwivedi and Xavier Bresson. 2020. A generalization of transformer networks to graphs. *arXiv* (2020).
- [13] William Fedus, Barret Zoph, and Noam Shazeer. 2022. Switch transformers: Scaling to trillion parameter models with simple and efficient sparsity. *Journal of Machine Learning Research* (2022).
- [14] Wenzheng Feng, Jie Zhang, Yuxiao Dong, Yu Han, Huanbo Luan, Qian Xu, Qiang Yang, Evgeny Kharlamov, and Jie Tang. 2020. Graph random neural networks for semi-supervised learning on graphs. *NeurIPS* (2020).
- [15] Justin Gilmer, Samuel S Schoenholz, Patrick F Riley, Oriol Vinyals, and George E Dahl. 2017. Neural message passing for quantum chemistry. In *ICML*.
- [16] Alex Graves. 2016. Adaptive computation time for recurrent neural networks. *arXiv* (2016).
- [17] Shurui Gui, Xiner Li, Limei Wang, and Shuiwang Ji. 2022. Good: A graph out-of-distribution benchmark. *Proceedings of the ACM Web Conference* (2022).
- [18] Will Hamilton, Zhitao Ying, and Jure Leskovec. 2017. Inductive representation learning on large graphs. *NeurIPS* (2017).
- [19] Kaveh Hassani and Amir Hosein Khasahmadi. 2020. Contrastive multi-view representation learning on graphs. In *ICML*.
- [20] Zhenyu Hou, Xiao Liu, Yukuo Cen, Yuxiao Dong, Hongxia Yang, Chunjie Wang, and Jie Tang. 2022. Graphmae: Self-supervised masked graph autoencoders. In *KDD*.
- [21] Weihua Hu, Matthias Fey, Marinka Zitnik, Yuxiao Dong, Hongyu Ren, Bowen Area Liu, Michele Catasta, and Jure Leskovec. 2020. Open graph benchmark: Datasets for machine learning on graphs. *Proceedings of the ACM Web Conference* (2020).
- [22] Robert A Jacobs, Michael I Jordan, Steven J Nowlan, and Geoffrey E Hinton. 1991. Adaptive mixtures of local experts. *Neural computation* (1991).
- [23] Wei Jin, Yao Ma, Xiaorui Liu, Xianfeng Tang, Suhang Wang, and Jiliang Tang. 2020. Graph structure learning for robust graph neural networks. In *KDD*.
- [24] Mingxuan Ju, Wenhao Yu, Tong Zhao, Chuxu Zhang, and Yanfang Ye. 2022. Grape: Knowledge graph enhanced passage reader for open-domain question answering. *arXiv* (2022).
- [25] Grigory Khromov and Sidak Pal Singh. 2023. Some fundamental aspects about lipschitz continuity of neural networks. *arXiv* (2023).
- [26] TN Kipf. 2016. Semi-supervised classification with graph convolutional networks. *arXiv* (2016).
- [27] Kezhi Kong, Guohao Li, Mucong Ding, Zuxuan Wu, Chen Zhu, Bernard Ghanem, Gavin Taylor, and Tom Goldstein. 2022. Robust optimization as data augmentation for large-scale graphs. In *CVPR*.
- [28] Guohao Li, Matthias Muller, Ali Thabet, and Bernard Ghanem. 2019. DeepGCNs: Can GCNs go as deep as CNNs?. In *ICCV*.
- [29] Haoyang Li, Xin Wang, Ziwei Zhang, and Wenwu Zhu. 2025. Out-of-distribution generalization on graphs: A survey. *TPAMI* (2025).
- [30] Haoyang Li, Ziwei Zhang, Xin Wang, and Wenwu Zhu. 2022. Learning invariant graph representations for out-of-distribution generalization. *NeurIPS* (2022).
- [31] Ziming Li, Youhuan Li, Yuyu Luo, Guoliang Li, and Chuxu Zhang. 2025. Graph Neural Networks for Databases: A Survey. *Corr* (2025).
- [32] Ziming Li, Xiaoming Wu, Zehong Wang, Jiazheng Li, Yijun Tian, Jinhe Bi, Yunpu Ma, Yanfang Ye, and Chuxu Zhang. 2026. Graph is a Substrate Across Data Modalities. *arXiv* (2026).
- [33] Hui Liu, Jiarui Feng, Lecheng Kong, Ningyue Liang, Dacheng Tao, Yixin Chen, and Muhan Zhang. 2023. One for all: Towards training one graph model for all classification tasks. *arXiv* (2023).
- [34] Zheyuan Liu, Chunhui Zhang, Yijun Tian, Erchi Zhang, Chao Huang, Yanfang Ye, and Chuxu Zhang. 2023. Fair graph representation learning via diverse mixture-of-experts. In *WWW*.
- [35] Takeru Miyato, Toshiki Kataoka, Masanori Koyama, and Yuichi Yoshida. 2018. Spectral normalization for generative adversarial networks. *arXiv* (2018).
- [36] Yiyue Qian, Chunhui Zhang, Yiming Zhang, Qianlong Wen, Yanfang Ye, and Chuxu Zhang. 2022. Co-modality graph contrastive learning for imbalanced node classification. *NeurIPS* (2022).
- [37] Jiezhong Qiu, Qibin Chen, Yuxiao Dong, Jing Zhang, Hongxia Yang, Ming Ding, Kuansan Wang, and Jie Tang. 2020. Gcc: Graph contrastive coding for graph neural network pre-training. In *KDD*.
- [38] Yu Rong, Wenbing Huang, Tingyang Xu, and Junzhou Huang. 2019. Dropedge: Towards deep graph convolutional networks on node classification. *arXiv* (2019).
- [39] Clemens Rosenbaum, Tim Klinger, and Matthew Riemer. 2017. Routing networks: Adaptive selection of non-linear functions for multi-task learning. *arXiv* (2017).
- [40] Shiori Sagawa, Pang Wei Koh, Tatsunori B Hashimoto, and Percy Liang. 2019. Distributionally robust neural networks for group shifts: On the importance of regularization for worst-case generalization. *arXiv* (2019).
- [41] Alvaro Sanchez-Gonzalez, Jonathan Godwin, Tobias Pfaff, Rex Ying, Jure Leskovec, and Peter Battaglia. 2020. Learning to simulate complex physics with graph networks. In *ICML*.
- [42] Franco Scarselli, Marco Gori, Ah Chung Tsoi, Markus Hagenbuchner, and Gabriele Monfardini. 2008. The graph neural network model. *IEEE transactions on neural networks* (2008).
- [43] David Sculley, Gary Holt, Daniel Golovin, Eugene Davydov, Todd Phillips, Dietmar Ebner, Vinay Chaudhary, Michael Young, Jean-Francois Crespo, and Dan Dennison. 2015. Hidden technical debt in machine learning systems. *NeurIPS* (2015).
- [44] Shai Shalev-Shwartz and Shai Ben-David. 2014. *Understanding machine learning: From theory to algorithms*.
- [45] Noam Shazeer, Azalia Mirhoseini, Krzysztof Maziarz, Andy Davis, Quoc Le, Geoffrey Hinton, and Jeff Dean. 2017. Outrageously large neural networks: The sparsely-gated mixture-of-experts layer. *arXiv* (2017).
- [46] David I Shuman, Sunil K Narang, Pascal Frossard, Antonio Ortega, and Pierre Vandergheynst. 2013. The emerging field of signal processing on graphs: Extending high-dimensional data analysis to networks and other irregular domains. *IEEE signal processing magazine* (2013).
- [47] Shantanu Thakoor, Corentin Tallec, Mohammad Gheorghiciuc, Mehdi Azabou, Eva L Dyer, Remi Munos, Petar Veličković, and Michal Valko. 2021. Large-scale representation learning on graphs via bootstrapping. *arXiv* (2021).
- [48] Yijun Tian, Kaiwen Dong, Chunhui Zhang, Chuxu Zhang, and Nitesh V Chawla. 2023. Heterogeneous graph masked autoencoders. In *AAAI*.
- [49] Aaron Van Den Oord, Oriol Vinyals, et al. 2017. Neural discrete representation learning. *Proceedings of the ACM Web Conference* (2017).
- [50] Petar Veličković, Guillem Cucurull, Arantxa Casanova, Adriana Romero, Pietro Lio, Yoshua Bengio, et al. 2017. Graph attention networks. *stat* (2017).
- [51] Petar Veličković, William Fedus, William L Hamilton, Pietro Lio, Yoshua Bengio, and R Devon Hjelm. 2018. Deep graph infomax. *arXiv* (2018).
- [52] Song Wang, Zhen Tan, Yaochen Shu, Chuxu Zhang, and Jundong Li. 2025. Generative Risk Minimization for Out-of-Distribution Generalization on Graphs. *TMLR* (2025).
- [53] Zehong Wang, Zheyuan Zhang, Nitesh Chawla, Chuxu Zhang, and Yanfang Ye. 2024. Gft: Graph foundation model with transferable tree vocabulary. *NeurIPS* (2024).
- [54] Zehong Wang, Zheyuan Zhang, Tianyi Ma, Nitesh V Chawla, Chuxu Zhang, and Yanfang Ye. 2025. Beyond Message Passing: Neural Graph Pattern Machine. In *ICML*.
- [55] Zehong Wang, Zheyuan Zhang, Tianyi Ma, Nitesh V Chawla, Chuxu Zhang, and Yanfang Ye. 2025. Towards Graph Foundation Models: Learning Generalities Across Graphs via Task-Trees. In *ICML*.

[56] Zehong Wang, Zheyuan Zhang, Tianyi Ma, Chuxu Zhang, and Yanfang Ye. 2025. Generative Graph Pattern Machine. In *NeurIPS*.

[57] Qianlong Wen, Mingxuan Ju, Zhongyu Ouyang, Chuxu Zhang, and Yanfang Ye. 2024. From coarse to fine: enable comprehensive graph self-supervised learning with multi-granular semantic ensemble. In *ICML*.

[58] Qianlong Wen, Zhongyu Ouyang, Chunhui Zhang, Yiyue Qian, Chuxu Zhang, and Yanfang Ye. 2024. GCVR: reconstruction from cross-view enable sufficient and robust graph contrastive learning. In *UAI*.

[59] Qitian Wu, Fan Nie, Chenxiao Yang, Tianyi Bao, and Junchi Yan. 2024. Graph out-of-distribution generalization via causal intervention. In *WWW*.

[60] Shirley Wu, Kaidi Cao, Bruno Ribeiro, James Zou, and Jure Leskovec. 2024. GraphMETRO: Mitigating Complex Graph Distribution Shifts via Mixture of Aligned Experts. *NeurIPS* (2024).

[61] Ying-Xin Wu, Xiang Wang, An Zhang, Xiangnan He, and Tat-Seng Chua. 2022. Discovering invariant rationales for graph neural networks. *arXiv* (2022).

[62] Zhenqin Wu, Bharath Ramsundar, Evan N Feinberg, Joseph Gomes, Caleb Geniesse, Aneesh S Pappu, Karl Leswing, and Vijay Pande. 2018. MoleculeNet: a benchmark for molecular machine learning. *Chemical science* (2018).

[63] Keyulu Xu, Weihua Hu, Jure Leskovec, and Stefanie Jegelka. 2018. How powerful are graph neural networks? *arXiv* (2018).

[64] Chengxuan Ying, Tianqi Cai, Shengjie Luo, Shuxin Zheng, Guolin Ke, Di He, Yanming Shen, and Tie-Yan Liu. 2021. Do transformers really perform badly for graph representation? *NeurIPS* (2021).

[65] Rex Ying, Ruining He, Kaifeng Chen, Pong Eksombatchai, William L Hamilton, and Jure Leskovec. 2018. Graph convolutional neural networks for web-scale recommender systems. In *KDD*.

[66] Yuning You, Tianlong Chen, Yongduo Sui, Ting Chen, Zhangyang Wang, and Yang Shen. 2020. Graph contrastive learning with augmentations. *Proceedings of the ACM Web Conference* (2020).

[67] Xiangchi Yuan, Yijun Tian, Chunhui Zhang, Yanfang Ye, Nitesh V Chawla, and Chuxu Zhang. 2024. Graph cross supervised learning via generalized knowledge. In *KDD*.

[68] Xiangchi Yuan, Chunhui Zhang, Yijun Tian, Yanfang Ye, and Chuxu Zhang. 2024. Mitigating emergent robustness degradation while scaling graph learning. In *ICLR*.

[69] Chuxu Zhang, Dongjin Song, Chao Huang, Ananthram Swami, and Nitesh V Chawla. 2019. Heterogeneous graph neural network. In *KDD*.

[70] Chunhui Zhang, Yijun Tian, Mingxuan Ju, Zheyuan Liu, Yanfang Ye, Nitesh Chawla, and Chuxu Zhang. 2022. Chasing all-round graph representation robustness: Model, training, and optimization. In *ICLR*.

[71] Jiani Zhang, Xingjian Shi, Junyuan Xie, Hao Ma, Irwin King, and Dit-Yan Yeung. 2018. Gaam: Gated attention networks for learning on large and spatiotemporal graphs. *arXiv* (2018).

[72] Xiang Zhang and Marinka Zitnik. 2020. Gnnguard: Defending graph neural networks against adversarial attacks. *NeurIPS* (2020).

[73] Jianan Zhao, Qianlong Wen, Mingxuan Ju, Chuxu Zhang, and Yanfang Ye. 2023. Self-supervised graph structure refinement for graph neural networks. In *WSDM*.

[74] Jianan Zhao, Qianlong Wen, Shiyu Sun, Yanfang Ye, and Chuxu Zhang. 2021. Multi-view self-supervised heterogeneous graph embedding. In *ECML-PKDD*.

[75] Yun Zhu, Haizhou Shi, Zhenshuo Zhang, and Siliang Tang. 2024. Mario: Model agnostic recipe for improving ood generalization of graph contrastive learning. In *WWW*.

[76] Yanqiao Zhu, Yichen Xu, Feng Enter Yu, Qiang Liu, Shu Wu, and Liang Wang. 2020. Deep graph contrastive representation learning. *arXiv* (2020).

[77] Daniel Zügner, Amir Akbarnejad, and Stephan Günnemann. 2018. Adversarial attacks on neural networks for graph data. In *KDD*.

A H1 details: definitions, assumptions, lemmas, and proofs

A.1 Definitions for H1

Definition A.1 (Static inference class \mathcal{H}_1). A predictor $f_\theta \in \mathcal{H}_1$ is trained once and deployed under frozen inference. At deployment, it applies the same computation rule to every input instance (no instance-wise routing or selection).

Definition A.2 (Two-component decomposition induced by the graph). Fix two operators $T_L(G)$ and $T_H(G)$ that decompose node features into two complementary components:

$$X_L := T_L(G)X, \quad X_H := T_H(G)X, \quad T_L(G) + T_H(G) = I. \quad (25)$$

For instance, $T_L(G)$ can be a low-pass graph filter and $T_H(G)$ a high-pass graph filter.

Definition A.3 (A witness subfamily for \mathcal{H}_1 via a global reliance parameter). Define a witness subfamily $\mathcal{H}_1^{\text{wit}} \subseteq \mathcal{H}_1$ consisting of static predictors of the form

$$f_\theta(G, X) := h_\theta(X_L + \eta_\theta X_H), \quad (26)$$

where $\eta_\theta \geq 0$ controls the reliance on the X_H component and h_θ is a task head. After training, the scalar η_θ is fixed and shared across all environments at deployment.

Definition A.4 (Slice-optimal OOD risk for \mathcal{H}_1). For $\alpha > 0$ and $\varepsilon \geq 0$, define

$$\beta_1(\alpha, \varepsilon) := \inf_{\theta \in \mathcal{H}_1: \mathcal{R}_{\text{fit}}(\theta) \leq \alpha, \mathcal{R}_{\text{stab}}(\theta) \leq \varepsilon} \mathcal{R}_{\text{ood}}(\theta). \quad (27)$$

Scope for the H1 analysis (feature perturbations only). This appendix specializes the perturbation set to the case without structural perturbations, i.e., $G' = G$. Equivalently, this sets the structure budget to $\rho_s = 0$. Accordingly, for $z = (G, X)$ define the admissible feature-perturbation set

$$B(G, X) := \{X' : (G, X') \in B((G, X))\}. \quad (28)$$

All stability bounds below take the supremum over $X' \in B(G, X)$.

A.2 Assumption and proof ingredients

ASSUMPTION 1 (HIGH-COMPONENT NECESSITY AND PERTURBATIONS). Fix $\alpha > 0$. There exist a reference distribution D_0 over (G, X) , a test environment $e_1 \in E_{\text{test}}$ with distribution D_{e_1} over $((G, X), y)$, and constants $\rho > 0$, $L_h > 0$ such that:

(i) (Fitting requires nontrivial reliance on the high component) There exists a monotone decreasing function $\psi_{\text{fit}} : [0, \infty) \rightarrow \mathbb{R}_+$ such that for any θ in (26),

$$\mathcal{R}_{\text{fit}}(\theta) \geq \psi_{\text{fit}}(\eta_\theta), \quad \text{and} \quad \psi_{\text{fit}}(0) > \alpha. \quad (29)$$

(ii) (A witness OOD environment also requires nontrivial reliance on the high component) There exists a monotone decreasing function $\psi_{e_1} : [0, \infty) \rightarrow \mathbb{R}_+$ such that for any θ in (26),

$$\mathbb{E}_{((G, X), y) \sim D_{e_1}} [\ell(f_\theta(G, X), y)] \geq \psi_{e_1}(\eta_\theta), \quad \text{and} \quad \psi_{e_1}(0) > 0. \quad (30)$$

(iii) (Admissible feature perturbations act on the high component) For $(G, X) \sim D_0$ and any (G, X') with $X' \in B(G, X)$,

$$X'_L = X_L, \quad \|X'_H - X_H\| \leq \rho, \quad (31)$$

where $\|\cdot\|$ is the representation-space norm used below.

(iv) (The task head is Lipschitz from representation norm to output metric) The head h_θ is L_h -Lipschitz from $(\cdot, \|\cdot\|)$ to (\cdot, d) , i.e.,

$$d(h_\theta(u), h_\theta(v)) \leq L_h \|u - v\| \quad \forall u, v. \quad (32)$$

REMARK 1 (GENERAL PERTURBATIONS AFFECTING BOTH COMPONENTS). Assumption 1(iii) is imposed for tractability and captures the regime where admissible perturbations predominantly alter the non-smooth component. The analysis extends to the more general case where both components change, e.g., $\|X'_L - X_L\| \leq \rho_L$ and $\|X'_H - X_H\| \leq \rho_H$, by replacing Lemma A.5 with the pointwise bound

$$\sup_{X' \in B(G, X)} d(f_\theta(G, X), f_\theta(G, X')) \leq L_h (\rho_L + \eta_\theta \rho_H). \quad (33)$$

LEMMA A.5 (STABILITY BUDGET UPPER BOUNDS η). Under Assumption 1(iii)-(iv), for any θ in (26),

$$\sup_{X' \in B(G, X)} d(f_\theta(G, X), f_\theta(G, X')) \leq L_h \eta_\theta \rho. \quad (34)$$

By the definition of $\mathcal{R}_{\text{stab}}$ as an expectation over the pointwise supremum,

$$\mathcal{R}_{\text{stab}}(\theta) \leq L_h \eta_\theta \rho. \quad (35)$$

Therefore, $\mathcal{R}_{\text{stab}}(\theta) \leq \varepsilon$ implies

$$\eta_\theta \leq \eta_{\text{max}}(\varepsilon) := \frac{\varepsilon}{L_h \rho}. \quad (36)$$

PROOF. Fix (G, X) and any $X' \in B(G, X)$. By (26),

$$f_\theta(G, X) = h_\theta(X_L + \eta_\theta X_H), \quad f_\theta(G, X') = h_\theta(X'_L + \eta_\theta X'_H).$$

Assumption 1(iii) gives $X'_L = X_L$ and $\|X'_H - X_H\| \leq \rho$, hence

$$\|(X_L + \eta_\theta X_H) - (X'_L + \eta_\theta X'_H)\| = \eta_\theta \|X_H - X'_H\| \leq \eta_\theta \rho.$$

By Assumption 1(iv),

$$d(f_\theta(G, X), f_\theta(G, X')) = d(h_\theta(X_L + \eta_\theta X_H), h_\theta(X'_L + \eta_\theta X'_H)) \leq L_h \cdot \eta_\theta \rho.$$

Taking the supremum over $X' \in B(G, X)$ yields (34). The bound (35) follows by taking expectation over $(G, X) \sim D_0$ under the definition of $\mathcal{R}_{\text{stab}}$. Finally, rearranging (35) under $\mathcal{R}_{\text{stab}}(\theta) \leq \varepsilon$ gives (36). \square

LEMMA A.6 (FITTING PREREQUISITE ENFORCES A MINIMUM η). Under Assumption 1(i), define

$$\eta_{\text{min}}(\alpha) := \inf\{\eta \geq 0 : \psi_{\text{fit}}(\eta) \leq \alpha\}. \quad (37)$$

Then for any θ in (26),

$$\mathcal{R}_{\text{fit}}(\theta) \leq \alpha \Rightarrow \eta_\theta \geq \eta_{\text{min}}(\alpha). \quad (38)$$

PROOF. Assumption 1(i) gives $\mathcal{R}_{\text{fit}}(\theta) \geq \psi_{\text{fit}}(\eta_\theta)$. If $\mathcal{R}_{\text{fit}}(\theta) \leq \alpha$, then $\psi_{\text{fit}}(\eta_\theta) \leq \alpha$ must hold. By the definition of $\eta_{\text{min}}(\alpha)$ in (37), this implies $\eta_\theta \geq \eta_{\text{min}}(\alpha)$. \square

A.3 Proof of the H1 witness-family limitation

THEOREM A.7 (A WITNESS-SUBFAMILY JOINT LIMITATION UNDER A STABILITY BUDGET). *Under Assumption 1, fix (α, ε) and define $\eta_{\max}(\varepsilon)$ and $\eta_{\min}(\alpha)$ as in (36) and (37).*

(a) *(Feasible slice implies a worst-environment lower bound within the witness subfamily)* If $\eta_{\min}(\alpha) \leq \eta_{\max}(\varepsilon)$, then for any θ in (26) satisfying both $\mathcal{R}_{\text{fit}}(\theta) \leq \alpha$ and $\mathcal{R}_{\text{stab}}(\theta) \leq \varepsilon$,

$$\mathcal{R}_{\text{ood}}(\theta) \geq \mathbb{E}_{D_{e_1}}[\ell(f_\theta(G, X), y)] \geq \psi_{e_1}(\eta_{\max}(\varepsilon)) =: \beta_{-1}(\alpha, \varepsilon), \quad (39)$$

and $\beta_{-1}(\alpha, \varepsilon) > 0$ under Assumption 1(ii).

(b) *(Incompatibility of fitting and stability within the witness subfamily)* If $\eta_{\min}(\alpha) > \eta_{\max}(\varepsilon)$, then no predictor in the witness subfamily (26) can simultaneously satisfy $\mathcal{R}_{\text{fit}}(\theta) \leq \alpha$ and $\mathcal{R}_{\text{stab}}(\theta) \leq \varepsilon$.

PROOF. (a) Lemma A.5 implies that $\mathcal{R}_{\text{stab}}(\theta) \leq \varepsilon$ yields $\eta_\theta \leq \eta_{\max}(\varepsilon)$. Since ψ_{e_1} is monotone decreasing, Assumption 1(ii) gives

$$\mathbb{E}_{((G, X), y) \sim D_{e_1}}[\ell(f_\theta(G, X), y)] \geq \psi_{e_1}(\eta_\theta) \geq \psi_{e_1}(\eta_{\max}(\varepsilon)),$$

and (39) follows by $\mathcal{R}_{\text{ood}}(\theta) \geq \mathbb{E}_{D_{e_1}}[\ell]$.

(b) Lemma A.6 implies that $\mathcal{R}_{\text{fit}}(\theta) \leq \alpha$ yields $\eta_\theta \geq \eta_{\min}(\alpha)$. Combining with $\eta_\theta \leq \eta_{\max}(\varepsilon)$ from Lemma A.5 shows feasibility requires $\eta_{\min}(\alpha) \leq \eta_{\max}(\varepsilon)$. If instead $\eta_{\min}(\alpha) > \eta_{\max}(\varepsilon)$, no θ in (26) can satisfy both constraints. \square

REMARK 2 (MAIN-TEXT SIMPLIFIED STATEMENT). *The main text states the same result in a merged form: if $\eta_{\min}(\alpha) > \eta_{\max}(\varepsilon)$ then the feasible slice is empty within $\mathcal{H}_1^{\text{wit}}$, otherwise any feasible $\theta \in \mathcal{H}_1^{\text{wit}}$ satisfies the lower bound $\mathcal{R}_{\text{ood}}(\theta) \geq \beta_{-1}(\alpha, \varepsilon)$ in (39).*

B H2 details: proofs and strict separation

This appendix provides the formal instantiations and proofs behind the two main-text handles: the coverage-plus-selection bound (11) and the routing decomposition bound (12). It also states a sufficient-conditions theorem (stabilized ICC regime), and a strict-separation corollary.

B.1 Finite witness-family instantiation for coverage and selection

Witness-family routed predictor. Consider a finite family of mechanisms $\mathcal{F} = \{f^{(k)}\}_{k \in \mathcal{K}}$ and a fixed, deterministic (possibly lossy) discretization map $\kappa : \mathcal{R} \rightarrow \mathcal{K}$. This induces a discrete selector

$$\tilde{r}_\theta(z) := \kappa(r_\theta(z)) \in \mathcal{K}, \quad (40)$$

and a routed predictor

$$f_\theta(z) := f^{(\tilde{r}_\theta(z))}(z). \quad (41)$$

The discretization κ is part of the witness-family instantiation and is not an additional learned routing mechanism.

Definition B.1 (Oracle index and selector error). For each $e \in E_{\text{test}}$, choose any minimizer

$$k^*(e) \in \arg \min_{k \in \mathcal{K}} \mathbb{E}_{(z, y) \sim D_e}[\ell(f^{(k)}(z), y)]. \quad (42)$$

Let $z \sim D_e$ denote the input marginal under D_e . Define the selector error as

$$\delta_{\text{sel}}(e) := \mathbb{P}_{z \sim D_e}[\tilde{r}_\theta(z) \neq k^*(e)]. \quad (43)$$

Definition B.2 (Coverage level). Define the coverage level as

$$\beta_{\text{cov}} := \sup_{e \in E_{\text{test}}} \min_{k \in \mathcal{K}} \mathbb{E}_{(z, y) \sim D_e}[\ell(f^{(k)}(z), y)]. \quad (44)$$

ASSUMPTION 2 (BOUNDED EVALUATION LOSS). *There exists $L_{\max} > 0$ such that $0 \leq \ell(\cdot, \cdot) \leq L_{\max}$ on the support of $\bigcup_{e \in E_{\text{test}}} D_e$ for the evaluation loss used in this appendix. This does not restrict training, which may use an unbounded surrogate.*

THEOREM B.3 (COVERAGE PLUS SELECTION CONTROLS WORST-ENVIRONMENT OOD RISK). *Under Definitions B.1–B.2 and Assumption 2, the witness-family routed predictor (41) satisfies, for every $e \in E_{\text{test}}$,*

$$\mathbb{E}_{(z, y) \sim D_e}[\ell(f_\theta(z), y)] \leq \beta_{\text{cov}} + L_{\max} \delta_{\text{sel}}(e),$$

and hence

$$\mathcal{R}_{\text{ood}}(\theta) \leq \beta_{\text{cov}} + L_{\max} \cdot \sup_{e \in E_{\text{test}}} \delta_{\text{sel}}(e). \quad (45)$$

PROOF. Fix any $e \in E_{\text{test}}$ and a minimizer $k^*(e)$ as in (42). Let $\mathcal{E} = \{\tilde{r}_\theta(z) = k^*(e)\}$ where z denotes the input marginal under D_e . Then

$$\begin{aligned} \mathbb{E}_{(z, y) \sim D_e}[\ell(f_\theta(z), y)] &= \mathbb{E}[\ell(f^{(k^*(e))}(z), y) \mid \mathcal{E}] \mathbb{P}(\mathcal{E}) \\ &\quad + \mathbb{E}[\ell(f^{(\tilde{r}_\theta(z))}(z), y) \mid \mathcal{E}^c] \mathbb{P}(\mathcal{E}^c). \end{aligned}$$

By the definition of $k^*(e)$, $\mathbb{E}_{(z, y) \sim D_e}[\ell(f^{(k^*(e))}(z), y)] \leq \beta_{\text{cov}}$. Also, by Assumption 2, $\mathbb{E}[\ell(f^{(\tilde{r}_\theta(z))}(z), y) \mid \mathcal{E}^c] \leq L_{\max}$. Finally, $\mathbb{P}(\mathcal{E}^c) = \delta_{\text{sel}}(e)$ by (43). Combining yields the per-environment bound, and taking $\sup_{e \in E_{\text{test}}}$ yields (45). \square

B.2 ICC stability decomposition: definitions and proof

Routing-fixed sensitivity and routing drift. Equip the routing space \mathcal{R} with a distance function $\text{dist}_{\mathcal{R}}$. Define the routing-fixed sensitivity

$$\mathcal{R}_{\text{base}}(\theta) := \mathbb{E}_{z \sim D_0} \left[\sup_{z' \in B(z)} d(F(r_\theta(z), z), F(r_\theta(z), z')) \right], \quad (46)$$

and the routing drift

$$\mathcal{R}_{\text{route}}(\theta) := \mathbb{E}_{z \sim D_0} \left[\sup_{z' \in B(z)} \text{dist}_{\mathcal{R}}(r_\theta(z), r_\theta(z')) \right]. \quad (47)$$

Execution sensitivity envelope. Define the pointwise routing envelope at input z as

$$L_F(z) := \sup_{\substack{r, r' \in \mathcal{R} \\ \text{dist}_{\mathcal{R}}(r, r') > 0}} \frac{d(F(r, z), F(r', z))}{\text{dist}_{\mathcal{R}}(r, r')}, \quad (48)$$

and define its perturbation-closed reference version as

$$L_F^B(D_0) := \mathbb{E}_{z \sim D_0} \left[\sup_{z' \in B(z)} L_F(z') \right]. \quad (49)$$

LEMMA B.4 (ICC STABILITY DECOMPOSITION). *Assume $L_F^B(D_0) < \infty$. Then for $f_\theta(z) = F(r_\theta(z), z)$,*

$$\mathcal{R}_{\text{stab}}(\theta) \leq \mathcal{R}_{\text{base}}(\theta) + L_F^B(D_0) \cdot \mathcal{R}_{\text{route}}(\theta). \quad (50)$$

PROOF. Fix z and any $z' \in B(z)$. Write $r = r_\theta(z)$ and $r' = r_\theta(z')$. By triangle inequality and adding/subtracting $F(r, z')$,

$$d(F(r, z), F(r', z')) \leq d(F(r, z), F(r, z')) + d(F(r, z'), F(r', z')).$$

Taking $\sup_{z' \in B(z)}$ and then $\mathbb{E}_{z \sim D_0}$, the first term yields $\mathcal{R}_{\text{base}}(\theta)$ by (46). For the second term, by (48),

$$d(F(r, z'), F(r', z')) \leq L_F(z') \cdot \text{dist}_{\mathcal{R}}(r, r').$$

Taking $\sup_{z' \in B(z)}$ and then $\mathbb{E}_{z \sim D_0}$ yields

$$\mathbb{E}_{z \sim D_0} \left[\sup_{z' \in B(z)} d(F(r, z'), F(r', z')) \right] \leq L_F^B(D_0) \cdot \mathcal{R}_{\text{route}}(\theta)$$

using (49) and (47). Combining proves (50). \square

REMARK 3 (INSTANTIATION EXAMPLES). Hard routing corresponds to $\mathcal{R} = \mathcal{K}$ with $\text{dist}_{\mathcal{R}}(k, k') = \mathbf{1}\{k \neq k'\}$, κ being the identity map, and $F(k, z) = f^{(k)}(z)$. Soft routing corresponds to $\mathcal{R} = \Delta(\mathcal{K})$ with $\text{dist}_{\mathcal{R}}$ taken as total variation or Wasserstein, and $F(\pi, z)$ defined as a mixture over mechanisms. In this case, the coverage-plus-selection analysis above uses a fixed discretization $\kappa(\pi)$ (e.g., top-1) to obtain $\tilde{r}_\theta(z) \in \mathcal{K}$.

B.3 Sufficient conditions for joint success

ASSUMPTION 3 (STABILIZED ROUTING CAPS). There exist $\bar{\delta}_{\text{sel}} \in [0, 1]$ and $\bar{\rho}_{\text{route}} \geq 0$ such that

$$\sup_{e \in E_{\text{test}}} \delta_{\text{sel}}(e) \leq \bar{\delta}_{\text{sel}}, \quad (51)$$

and

$$\mathcal{R}_{\text{route}}(\theta) \leq \bar{\rho}_{\text{route}}, \quad (52)$$

where $\delta_{\text{sel}}(e)$ is from (43) and $\mathcal{R}_{\text{route}}(\theta)$ from (47).

ASSUMPTION 4 (CONTROLLED EXECUTION CAPS). There exist $\bar{\varepsilon}_{\text{base}} \geq 0$ and $\bar{L}_F \geq 0$ such that

$$\mathcal{R}_{\text{base}}(\theta) \leq \bar{\varepsilon}_{\text{base}}, \quad (53)$$

and

$$L_F^B(D_0) \leq \bar{L}_F, \quad (54)$$

where $\mathcal{R}_{\text{base}}(\theta)$ is in (46) and $L_F^B(D_0)$ in (49).

THEOREM B.5 (SUFFICIENT CONDITIONS FOR JOINT SUCCESS). Assume Assumption 2 and Definitions B.1–B.2. If Assumptions 3 and 4 hold, then

$$\mathcal{R}_{\text{ood}}(\theta) \leq \beta_{\text{cov}} + L_{\text{max}} \cdot \bar{\delta}_{\text{sel}}, \quad (55)$$

and

$$\mathcal{R}_{\text{stab}}(\theta) \leq \bar{\varepsilon}_{\text{base}} + \bar{L}_F \cdot \bar{\rho}_{\text{route}}. \quad (56)$$

PROOF. The OOD bound follows by combining Theorem B.3 with (51). The stability bound follows by combining Lemma B.4 with (52), (53), and (54). \square

B.4 Strict separation on a feasible slice (against the H1 witness family)

COROLLARY B.6 (STRICT SEPARATION ON A FEASIBLE SLICE (AGAINST THE H1 WITNESS FAMILY)). Assume the conditions of Theorem B.5 hold, and let $\underline{\beta}_1(\alpha, \varepsilon)$ be the H1 witness-family lower bound in Theorem 3.1. If

$$\beta_{\text{cov}} + L_{\text{max}} \cdot \bar{\delta}_{\text{sel}} < \underline{\beta}_1(\alpha, \varepsilon), \quad (57)$$

then

$$\beta_2(\alpha, \varepsilon) < \underline{\beta}_1(\alpha, \varepsilon), \quad (58)$$

i.e., ICC strictly improves worst-environment OOD risk over the H1 witness family on the same slice.

PROOF. By Theorem B.5, there exists a feasible $\theta \in \mathcal{H}_2$ whose worst-environment risk is at most $\beta_{\text{cov}} + L_{\text{max}} \bar{\delta}_{\text{sel}}$. Under (57), this is strictly below $\underline{\beta}_1(\alpha, \varepsilon)$. Taking the infimum over feasible θ in the definition of $\beta_2(\alpha, \varepsilon)$ yields (58). \square

C Method details

C.1 Proof of Lemma 4.1

PROOF. Fix an input instance z and a node $v \in V$. Let

$$j^\star := q_\theta(v; z) = \arg \min_{1 \leq j \leq M} \|u_v(z) - c_j\|_2,$$

and recall the margin

$$m_v(z) := \min_{j \neq j^\star} \|u_v(z) - c_j\|_2 - \|u_v(z) - c_{j^\star}\|_2.$$

Assume that for all $z' \in B(z)$,

$$\|u_v(z') - u_v(z)\|_2 < \frac{1}{2} m_v(z).$$

Consider any admissible $z' \in B(z)$ and any competitor code $j \neq j^\star$. By the triangle inequality,

$$\|u_v(z') - c_{j^\star}\|_2 \leq \|u_v(z) - c_{j^\star}\|_2 + \|u_v(z') - u_v(z)\|_2,$$

and

$$\|u_v(z') - c_j\|_2 \geq \|u_v(z) - c_j\|_2 - \|u_v(z') - u_v(z)\|_2.$$

Let $\delta := \|u_v(z') - u_v(z)\|_2$. By the triangle inequality,

$$\|u_v(z') - c_{j^\star}\|_2 \leq \|u_v(z) - c_{j^\star}\|_2 + \delta,$$

$$\|u_v(z') - c_j\|_2 \geq \|u_v(z) - c_j\|_2 - \delta.$$

Hence, for any $j \neq j^\star$,

$$\|u_v(z') - c_j\|_2 - \|u_v(z') - c_{j^\star}\|_2 \geq m_v(z) - 2\delta > 0,$$

where the last step uses $\delta < \frac{1}{2} m_v(z)$. Therefore $q_\theta(v; z') = q_\theta(v; z)$, where the last inequality uses $\|u_v(z') - u_v(z)\|_2 < \frac{1}{2} m_v(z)$. Hence,

$$\|u_v(z') - c_{j^\star}\|_2 < \|u_v(z') - c_j\|_2 \quad \forall j \neq j^\star,$$

so the nearest-code assignment is unchanged: $q_\theta(v; z') = j^\star = q_\theta(v; z)$.

Since the condition holds for every node $v \in V$, token indices are invariant on $B(z)$, and thus the tokenized interface is invariant: $Q(u_\theta(z')) = Q(u_\theta(z))$ for all $z' \in B(z)$. \square

C.2 Proof of Proposition 4.2

Let $C = \{c_j\}_{j=1}^M$ be the VQ codebook and define its diameter

$$\text{diam}(C) := \max_{i,j} \|c_i - c_j\|_2.$$

Let the token embedding for node v be $\tilde{u}_v(z) = Q(u_v(z)) \in C$.

Node-level tasks (no pooling). For any $z' \in B(z)$ and any node v , both $\tilde{u}_v(z')$ and $\tilde{u}_v(z)$ lie in C , hence

$$\|\tilde{u}_v(z') - \tilde{u}_v(z)\|_2 \leq \text{diam}(C).$$

Since the head is L -Lipschitz under $\|\cdot\|_2$,

$$\|f_t(\tilde{u}_v(z')) - f_t(\tilde{u}_v(z))\|_2 \leq L\|\tilde{u}_v(z') - \tilde{u}_v(z)\|_2 \leq L \text{diam}(C).$$

Graph-level tasks (with pooling). Let $A(z) = \{\tilde{u}_v(z)\}_{v \in V}$ denote the token set. Assume the pooling operator is L_{pool} -Lipschitz with respect to the nodewise norm

$$\|A\|_{V,2} := \left(\frac{1}{|V|} \sum_{v \in V} \|a_v\|_2^2 \right)^{1/2},$$

namely,

$$\|\text{Pool}(A) - \text{Pool}(B)\|_2 \leq L_{\text{pool}}\|A - B\|_{V,2}.$$

The per-node bound $\|\tilde{u}_v(z') - \tilde{u}_v(z)\|_2 \leq \text{diam}(C)$ implies

$$\|A(z') - A(z)\|_{V,2} \leq \text{diam}(C).$$

Let $r(z) = \text{Pool}(A(z))$. Then

$$\|r(z') - r(z)\|_2 \leq L_{\text{pool}} \text{diam}(C),$$

and by the L -Lipschitzness of f_t ,

$$\|f_t(r(z')) - f_t(r(z))\|_2 \leq L\|r(z') - r(z)\|_2 \leq L L_{\text{pool}} \text{diam}(C).$$

This matches Eq. (24) up to the pooling factor for graph-level tasks. \square

D Experimental Details and Additional Results

D.1 Datasets and Splits

Table 5 summarizes the dataset statistics. For CORA and PUBMED, we follow the common semi-supervised split protocol with 20 labeled nodes per class for training, and report the average performance over 10 predefined splits (different random seeds). For WIKICS, we use the standard split setting and average results over the 20 official splits. For ARXIV and the molecule benchmarks (HIV, PCBA, ChEMBL), we follow the official splits released with the corresponding benchmarks and repeat each experiment 10 times with different random seeds. For the knowledge graph benchmarks (FB15K237 and WN18RR), we adopt the standard fixed splits from prior work (e.g., [33]) and repeat each experiment 10 times with random seeds. Concretely, FB15K237 contains 272,115 training edges, 17,535 validation edges, and 20,466 test edges, while WN18RR contains 86,835 training edges, 3,034 validation edges, and 3,134 test edges. Unless otherwise specified, we report mean and standard deviation across repeated runs.

Table 5: Dataset statistics [33].

Dataset	Domain	Task	#Graphs	Avg. #Nodes	Avg. #Edges	#Classes
Cora	Citation	Node	1	2,708	10,556	7
PubMed	Citation	Node	1	19,717	44,338	3
Arxiv	Citation	Node	1	169,343	1,166,243	40
WikiCS	Web link	Node	1	11,701	216,123	10
FB15K237	Knowledge	Link	1	14,541	310,116	237
WN18RR	Knowledge	Link	1	40,943	93,003	11
PCBA	Molecule	Graph	437,929	26.0	28.1	128
HIV	Molecule	Graph	41,127	25.5	27.5	2
ChEMBL	Molecule	Graph	365,065	25.9	55.9	1,048

D.2 Inference-time Feature Masking

Masking rule. We evaluate feature robustness by randomly masking input node features at inference time while keeping the trained model fixed. Given a node feature matrix $X \in \mathbb{R}^{n \times d}$, we apply element-wise missingness on the evaluation nodes: for each evaluation node v and each feature dimension $j \in [d]$, we sample an independent Bernoulli mask $m_{v,j} \sim \text{Bernoulli}(p)$ (with fixed masking rate p) and set the masked entries to zero, leaving others unchanged. Non-evaluation nodes remain unchanged. Formally,

$$X'_{v,j} = \begin{cases} 0, & m_{v,j} = 1, \\ X_{v,j}, & m_{v,j} = 0, \end{cases} \quad X'_{v,j} = X_{v,j} \text{ for } v \notin \mathcal{V}_{\text{eval}}.$$

D.3 Inference-time Random Edge Drop

Edge-drop rule. We evaluate structural robustness by randomly deleting edges at inference time while keeping the trained model fixed. Given an input graph $G = (V, E)$, we first canonicalize the adjacency into a simple undirected edge set (merge reciprocal directions and remove duplicates). We then form the candidate set as edges that touch the evaluation nodes, and independently drop a subset of these candidate edges with a fixed drop rate. When an undirected edge is selected, both directions are removed together to preserve symmetry. The implementation also prevents the degenerate case where all candidate edges are deleted in a single sample.

D.4 Degree-based OOD Evaluation

Degree buckets. We create an OOD shift by partitioning nodes according to (undirected) degree. We symmetrize the graph, compute degrees, sort nodes, and define three buckets: the lowest-degree 15% as OOD-low, the highest-degree 15% as OOD-high, and the remaining nodes as ID.

Split protocol. This evaluation does *not* use the dataset’s original train/val/test split. Instead, we only split nodes inside the ID bucket. Within ID, we perform a class-stratified split into ID-train, ID-val, and ID-test so that each class has at least one node in each split whenever feasible. The default split ratios are 50%/25%/25% (train/val/test) within each class; if a class is too small to satisfy all three parts under this ratio, we fall back to 60%/20%/20% and otherwise enforce a minimal 1/1/($n - 2$) allocation.

Training and evaluation. We train and early-stop using ID-train/ID-val only. After selecting the best checkpoint by ID-val, we report

accuracy on ID-test and also on OOD-low and OOD-high (which are never used for training or selection).

D.5 Feature-homophily OOD Evaluation

Feature-homophily score. We define a per-node feature-homophily score using the average cosine similarity between a node feature vector and its 1-hop neighbors. Let $x_v \in \mathbb{R}^d$ be the node feature and $\tilde{x}_v = x_v / \|x_v\|_2$ its ℓ_2 -normalized version. On the undirected, self-loop-free graph, we assign each edge (v, u) a cosine similarity

$$s_{vu} = \langle \tilde{x}_v, \tilde{x}_u \rangle.$$

The feature-homophily score of node v is the mean similarity over its 1-hop neighborhood:

$$h(v) = \frac{1}{|\mathcal{N}(v)|} \sum_{u \in \mathcal{N}(v)} s_{vu}.$$

If $|\mathcal{N}(v)| = 0$, $h(v)$ is undefined and v is excluded from the bucket construction.

Validity filtering. Nodes with invalid features (non-finite entries or zero norm) are excluded from homophily computation. We also exclude nodes that have no remaining valid-feature neighbors after filtering, since their homophily score would be undefined. Buckets are constructed only from the remaining valid nodes.

Buckets and OOD split. We sort valid nodes by their feature-homophily score and define three buckets: the lowest-scoring 15% as OOD-low, the highest-scoring 15% as OOD-high, and the remaining nodes as ID.

Split protocol. This evaluation does *not* use the dataset’s original train/val/test split. Instead, we only split labeled nodes inside the ID bucket. Within ID, we perform a class-stratified split into ID-train, ID-val, and ID-test so that each class has at least one node in each split whenever feasible. The default per-class split ratios are 50%/25%/25% (train/val/test); when a class is too small, we fall back to 60%/20%/20% and otherwise enforce a minimal $1/1/(n-2)$ allocation. Additionally, ID nodes from classes with fewer than three samples in the ID bucket are dropped to avoid degenerate splits.

Training and evaluation. We train and early-stop using ID-train/ID-val only. After selecting the best checkpoint by ID-val, we report accuracy on ID-test and also on OOD-low and OOD-high (restricted to labeled nodes).

D.6 Tri-objective Evaluation

Feature-structure alignment score. On the undirected evaluation graph (self-loops removed), we define a per-node alignment score as the mean cosine similarity to 1-hop neighbors. Let $\tilde{x}_v = x_v / \|x_v\|_2$ and

$$a(v) = \frac{1}{|\mathcal{N}(v)|} \sum_{u \in \mathcal{N}(v)} \langle \tilde{x}_v, \tilde{x}_u \rangle.$$

Intuitively, larger $a(v)$ indicates stronger agreement between node features and local graph connectivity (feature-homophily), while smaller or negative values indicate weaker alignment. This score is used as an auxiliary statistic to characterize how closely the observed features conform to the neighborhood structure in each evaluation bucket. Nodes with invalid features, zero norm, or no valid-feature neighbors are excluded when computing $a(v)$.

Table 6: Ablation study on clean graphs (mean \pm std). Best per row is **bold, second best is underlined.**

Dataset	Full	w/o MoE	w/o Lip	w/o VQ
Cora	79.53 \pm 1.32	78.41 \pm 1.37	<u>79.11</u> \pm 1.58	78.28 \pm 1.38
PubMed	77.84 \pm 1.66	<u>77.59</u> \pm 1.28	76.92 \pm 1.40	77.07 \pm 1.27
WikiCS	80.11 \pm 0.53	79.29 \pm 0.59	<u>79.76</u> \pm 0.38	79.70 \pm 0.39
Arxiv	72.31 \pm 0.25	71.85 \pm 0.23	<u>71.96</u> \pm 0.32	70.67 \pm 0.10
WN18RR	92.34 \pm 0.25	<u>91.93</u> \pm 0.24	91.34 \pm 0.23	82.73 \pm 0.26
FB15K237	<u>90.26</u> \pm 0.16	89.27 \pm 0.11	89.86 \pm 0.14	92.39 \pm 0.13
HIV	73.54 \pm 1.02	<u>72.32</u> \pm 0.97	69.77 \pm 1.68	72.23 \pm 0.85
PCBA	<u>80.39</u> \pm 0.38	79.39 \pm 0.87	78.23 \pm 0.47	80.66 \pm 0.85
Avg.	80.79	<u>80.01</u>	79.62	79.22

OOD buckets (how we split). We sort all valid nodes by $a(v)$ in ascending order (lower means worse feature-structure alignment). We then take the bottom 10%, 10–20%, and 20–30% segments as three progressively less extreme OOD buckets:

$$\text{OOD3} = \text{bottom 10\%}, \quad \text{OOD2} = 10\text{--}20\%, \quad \text{OOD1} = 20\text{--}30\%.$$

The ID bucket is defined as the mid-range 30–80% segment:

$$\text{ID} = 30\text{--}80\%.$$

(Thus, higher-alignment nodes in the top 20% are not used in this protocol.)

ID re-splitting and metrics. For each run, we re-split *only the ID bucket* into train/val/ID-test using a label-stratified split (unlabeled nodes and ID classes with < 3 samples are filtered so every split is valid). All OOD buckets are kept fixed and used only for evaluation, so model selection never accesses shifted environments. Model selection is based on ID-val only (best checkpoint by validation accuracy). Using the selected checkpoint, we report: Fit = accuracy on clean ID-test; OOD = the *worst-bucket* accuracy across OOD1/OOD2/OOD3 on clean inputs. This worst-bucket metric directly reflects robustness under frozen deployment by emphasizing the most challenging shift rather than the average case.

Perturbation (missing-feature masking). We evaluate feature robustness by masking ID-test node features at inference time with element-wise missingness rates

$$p \in \{0.2, 0.4, 0.6, 0.8\},$$

where each entry is set to zero independently with probability p (the model is fixed and no test-time updates are performed). This perturbation is applied only at inference time and keeps the graph structure unchanged, isolating robustness to feature corruption. We report accuracy at each p , and define

$$\text{Perturb-mean} = \frac{1}{4} \sum_{p \in \{0.2, 0.4, 0.6, 0.8\}} \text{Acc}(p),$$

which summarizes performance across a spectrum from mild to severe missingness. For additional diagnostic signal, one can also view the relative degradation $\Delta(p) = \text{Acc}(\text{clean}) - \text{Acc}(p)$, but the main metric we use is Perturb-mean.

Table 7: Fine-tuning hyper-parameters for node benchmarks under different evaluation settings. Values are reported per dataset (Cora/PubMed/WikiCS).

Hyper-parameters	Missing-Feature Masking			Edge Dropping			Degree Shift			Homophily Shift			Tri-objective		
	Cora	PubMed	WikiCS	Cora	PubMed	WikiCS	Cora	PubMed	WikiCS	Cora	PubMed	WikiCS	Cora	PubMed	WikiCS
Learning Rate	7.5e-3	8e-4	5e-3	7.5e-3	5e-3	5e-3	1e-3	1.2e-3	2e-3	1e-3	3e-3	2e-3	3e-3	3e-3	3e-3
# Epochs	1,000	1,000	2,000	1,000	1,000	2,000	1,000	1,000	2,000	1,000	1,000	2,000	1,000	1,000	2,000
Early Stop	200	200	500	200	200	500	200	200	500	200	200	500	200	200	500
# MoE Experts (K)	3	3	3	3	3	3	3	3	3	3	3	3	3	3	3
Router Temperature (τ)	1.5	1.0	1.0	1.5	1.0	1.0	1.0	1.5	1.5	0.7	2.0	1.5	0.9	0.9	0.7
Dropout	0.90	0.90	0.50	0.90	0.50	0.50	0.90	0.80	0.90	0.90	0.80	0.90	0.90	0.80	0.80
Lipschitz Weight (λ_{lip})	5e-6	2e-3	3e-5	5e-6	2e-3	3e-5	4e-5	2e-3	3e-5	2.5e-4	1e-5	1e-3	5e-5	5e-5	5e-5

Table 8: Feature noise (missing-feature masking): node classification accuracy (%) under i.i.d. Bernoulli masking with rate α on evaluation nodes (masked values set to 0). Best per column is bold, second best is underlined.

Method	Cora			PubMed			WikiCS			Avg.
	$\alpha=0.4$	$\alpha=0.5$	$\alpha=0.6$	$\alpha=0.4$	$\alpha=0.5$	$\alpha=0.6$	$\alpha=0.4$	$\alpha=0.5$	$\alpha=0.6$	
CaNet[59]	73.86 \pm 1.38	72.69 \pm 1.75	71.90 \pm 1.94	73.81 \pm 1.30	72.67 \pm 1.66	72.23 \pm 2.29	77.34 \pm 0.70	76.87 \pm 0.67	76.12 \pm 0.72	74.17
GraphMETRO[60]	72.94 \pm 3.75	72.24 \pm 3.38	71.71 \pm 2.94	73.92 \pm 2.23	72.91 \pm 2.17	73.23 \pm 1.91	68.89 \pm 2.54	65.85 \pm 2.95	57.24 \pm 5.15	69.88
MARIO [75]	76.35 \pm 1.78	75.22 \pm 1.88	73.10 \pm 2.00	75.62 \pm 2.03	74.33 \pm 1.63	73.82 \pm 1.43	78.05 \pm 0.84	77.05 \pm 1.24	76.66 \pm 0.87	75.58
GFT[53]	74.70 \pm 1.75	72.26 \pm 5.39	67.74 \pm 8.01	74.49 \pm 1.40	73.33 \pm 1.36	71.47 \pm 1.43	75.77 \pm 1.21	72.81 \pm 2.22	68.77 \pm 3.23	72.37
TFEGNN[11]	76.64 \pm 1.31	<u>75.38</u> \pm 1.52	74.29 \pm 2.40	74.38 \pm 1.67	73.95 \pm 1.65	72.93 \pm 1.81	74.16 \pm 1.61	73.21 \pm 1.17	73.02 \pm 2.50	74.22
STEM-GNN	77.57 \pm 1.82	<u>75.98</u> \pm 1.73	<u>73.77</u> \pm 2.47	75.83 \pm 1.60	74.50 \pm 2.14	74.32 \pm 1.91	78.26 \pm 0.66	77.61 \pm 0.99	76.33 \pm 0.74	76.02

Table 9: Structural noise (edge deletion): node classification accuracy (%) under random undirected edge deletion with rate $p \in \{0.4, 0.5, 0.6\}$ on evaluation nodes. Best per column is bold, second best is underlined.

Method	Cora			PubMed			WikiCS			Avg.
	$p=0.4$	$p=0.5$	$p=0.6$	$p=0.4$	$p=0.5$	$p=0.6$	$p=0.4$	$p=0.5$	$p=0.6$	
CaNet[59]	72.34 \pm 1.77	70.69 \pm 2.08	69.33 \pm 1.99	73.17 \pm 1.36	72.74 \pm 1.43	72.46 \pm 1.35	76.45 \pm 0.58	<u>76.22</u> \pm 0.56	<u>75.60</u> \pm 0.60	73.22
GraphMETRO[60]	73.53 \pm 1.63	<u>71.93</u> \pm 1.24	70.51 \pm 1.63	73.41 \pm 1.48	72.49 \pm 1.97	72.05 \pm 1.85	73.85 \pm 1.08	72.93 \pm 1.47	72.09 \pm 1.24	72.53
MARIO [75]	<u>75.10</u> \pm 1.27	<u>73.08</u> \pm 1.53	<u>70.90</u> \pm 1.40	75.28 \pm 1.90	<u>75.16</u> \pm 1.85	<u>74.80</u> \pm 1.62	76.35 \pm 0.65	75.24 \pm 0.69	74.57 \pm 0.87	<u>74.50</u>
GFT[53]	73.64 \pm 1.86	71.91 \pm 2.17	70.04 \pm 2.51	<u>75.46</u> \pm 1.69	75.11 \pm 1.75	71.47 \pm 1.43	<u>76.46</u> \pm 0.75	75.60 \pm 0.86	74.32 \pm 1.14	73.78
TFEGNN [11]	73.44 \pm 1.79	72.12 \pm 1.68	70.12 \pm 1.76	73.51 \pm 1.62	73.02 \pm 1.67	72.52 \pm 1.71	74.89 \pm 1.03	75.20 \pm 1.09	74.53 \pm 1.29	73.26
STEM-GNN	75.15 \pm 0.96	73.10 \pm 1.15	71.05 \pm 1.78	75.68 \pm 1.54	75.64 \pm 1.55	75.45 \pm 1.77	77.49 \pm 0.52	76.53 \pm 0.63	75.74 \pm 0.80	75.09

Table 10: Hyper-parameters in fine-tuning.

Hyper-parameters	Cora	PubMed	Arxiv	WikiCS	WN18RR	FB15K237	HIV	PCBA
Learning Rate	7.5e-3	1.2e-3	5e-3	1.5e-2	1e-3	5e-4	7.5e-3	8e-4
# Epochs	1,000	1,000	1,000	2,000	1,000	3,000	100	50
Early Stop	200	200	200	500	200	200	20	10
Batch Size	0	0	0	0	0	1,024	1,024	1,024
# MoE Experts (K)	3	3	3	3	3	3	3	3
Router Temperature (τ)	0.9	1.5	1.2	1.2	2.0	1.0	0.9	1.0
Dropout	0.80	0.80	0.80	0.90	0.40	0.40	0.80	0.30
Lipschitz Weight (λ_{lip})	2.5e-5	7e-4	1e-4	1e-3	1e-4	1e-6	2.5e-5	1e-6

D.7 Hyperparameters

Pre-training of STEM-GNN. We pre-train STEM-GNN with a two-layer message-passing encoder (hidden dimension 768) using ReLU and batch normalization. We enable vector quantization with code-book size $M=128$ and token dimension $d_q=768$. The encoder uses an

MoE in the last layer with $K=3$ experts and Gumbel-Softmax routing ($\tau=1.0$). We optimize with AdamW (lr 1e-4, weight decay 1e-5) for 25 epochs with batch size 1024. Pre-training uses edge/feature drop augmentation (rate 0.2) and reconstructs 10% of links with an equal number of negatives; the semantic sampling factor is $\gamma=1$.

Fine-tuning of STEM-GNN. We fine-tune STEM-GNN with AdamW under the frozen-deployment protocol, using dataset-specific learning rates, epochs, and early-stopping patience (Table 10 and Table 7). We freeze VQ (freeze_vq=1) and optimize the MoE encoder together with a linear task head. We fix the MoE capacity to $K=3$ experts and apply MoE only on the last encoder layer, tuning the router temperature τ and dropout per dataset. Fine-tuning uses a Lipschitz penalty weighted by λ_{lip} on the head.